2

POLARIMETRIC SIGNATURES OF RANDOM DISCRETE SCATTERERS BASED ON VECTOR RADIATIVE TRANSFER THEORY

L. Tsang, K. H. Ding, and B. Wen

2.1 Introduction

Recently there has been increasing interest in the applications of polarimetry to microwave remote sensing of geophysical terrain [1–10]. Using radar polarimetry, the copolarization and depolarization return for arbitrary elliptical polarized incident wave can be measured. Some of the prominent features in terrain signatures are a pedestal in copolarization return, exhibition of partial polarization on averaging of the return signals, and a phase difference between vv and hh polarized waves. In this chapter, we model the terrain as discrete scatterers that are randomly distributed and are governed by orientation and size distributions. The polarimetric signatures are calculated by using the vector radiative transfer theory [11]. Two cases are considered: Sparse nonspherical particles and dense media with appreciable fractional volume of spherical particles of multiple sizes and permittivities.

In part I we consider a layer of nonspherical particles that are sparsely distributed and is overlying a homogeneous half space. We use the vector radiative transfer theory with a general nondiagonal extinction matrix and a phase matrix that are averaged over particle sizes and orientations [11–17]. Incident waves with general elliptical polarizations are considered in the scattering problem. In sections 2.2a and 2.2b, we discuss properties of the extinction matrix and also give conditions on the scattering amplitudes that must be satisfied before they can be used in calculation of the extinction matrix elements. In section 2.2c we discuss the properties of phase matrix in relation to polarimetric signatures. In sections 2.2d and 2.2e we list the first order multiple scattering and second order multiple scattering solution of the Mueller matrix. The Mueller matrix as calculated in this manner is an ensemble-averaged quantity due to the inherent nature of the radiative transfer theory. The copolarization, depolarization, phase difference and degree of polarization are then calculated using this ensemble averaged Mueller matrix. We also discuss the differences between single scattering and the first order multiple scattering solution. The solutions are expressed in terms of the phase matrix and the eigenmatrix of the extinction matrix. In section 2.2f, numerical results of copolarization return, depolarization return, phase difference between scattered vv and hh waves, and the degree of polarization are illustrated. Some of the salient features of the results are as follows. (i) The inclusion of the nondiagonal extinction matrix allows the vector radiative transfer theory to yield an appreciable phase difference between vv and hh

polarizations particularly for aligned scatterers. The phase difference decreases with increasing variance of orientation of the scatterers. (ii) The scattered Stokes vector on ensemble averaging is generally partially polarized with a degree of polarization less than unity. There is a big difference of degree of polarization between the case of aligned scatterers and the case of randomly oriented scatterers. (iii) There generally exists a pedestal in the copolarization return when plotted as a function of ellipticity and orientation angles. (iv) The factors that affect significantly the polarization signatures are the orientation distributions of the particles, the differences between the two effective propagation constants as expressed in the elements of the extinction matrix, and the contributions of multiple scattering effects for media with appreciable albedo and optical thickness. In the appendix, we list the extinction and phase matrices of small spheroids that are uniformly oriented in Euler angle γ and follow prescribed distribution in Euler angle β.

In part II, we apply the dense media radiative transfer theory to study the polarimetric signatures of a medium containing a high concentration of spherical particles with sizes governed by a particle size distribution [11, 18–22]. In a dense medium, the assumption of independent scattering, that is used in conventional radiative transfer theory is not valid [23]. This has been verified by controlled laboratory experiments in which the scattering properties of the medium are measured as a function of concentration of particles [24–26]. The experimental data indicate that, in a dense medium with small particles, both the attenuation rate and the bistatic intensity first increase with volume fraction of particles until a maximum is reached, and then decrease when the volume fraction further increases [24–26]. To explain the phenomenon, we used a dense medium radiative transfer theory that takes into account correlated scattering [11, 18, 19, 22]. The dense medium radiative transfer equations are derived from the Dyson's equation under the quasicrystalline approximation with coherent potential (QCA–CP) and Bethe-Salpeter equation under ladder approximation of correlated scatterers [18, 22]. The conditional probability of particle positions for media with identical sizes and media with particle size distributions are calculated by using the Percus-Yevick approximation [20, 21, 27–29] which are in good agreement with Monte Carlo simulations [30] and laboratory simulations [31]. The dense medium theory explains the laboratory data [10]. In section 2.3a, we give the governing equations for

calculating the effective propagation constants, extinction rates and scattering albedo for a dense medium with particle size distribution and multiple permittivities. Correlated scattering effects are included through the pair distribution functions which are calculated by the Percus-Yevick approximation. In sections 2.3b and 2.3c we discuss the dense medium vector radiative transfer equations and the steps of calculating the multiple scattering solutions. The full multiple scattering effects are studied as the radiative transfer equations are solved numerically. In section 2.3d we compare the results of dense medium theory with laboratory experiments. In section 2.3e we illustrate numerical results of radar polarimetry. It is shown that multiple scattering effects can decrease the degree of polarization. Multiple scattering also gives rise to a pedestal in the copolarization signature.

2.2 Part I. Nonspherical Particles

a. Vector Radiative Transfer Theory for a Layer of Sparsely Distributed Nonspherical Particles

Consider a collection of sparsely distributed nonspherical particles with permittivity ϵ_s embedded in a background medium with permittivity ϵ (region 1) overlying a homogeneous dielectric of permittivity ϵ_2 (region 2). An incident wave is launched from region 0 in direction $(\pi - \theta_o, \phi_o)$. Region 0 has permittivity ϵ which is the same as that of the background medium of region 1 (Fig. 2.1).

The vector radiative transfer equation in region 1 is of the following form [11]. For $0 \leq \theta \leq \pi$, $0 \leq \phi \leq 2\pi$

$$\cos\theta \frac{d}{dz}\overline{I}(\theta,\phi,z) = -\overline{\overline{\kappa_e}}(\theta,\phi)\cdot\overline{I}(\theta,\phi,z) + \int_0^{2\pi} d\phi' \int_0^{\pi} d\theta' \sin\theta' \overline{\overline{P}}(\theta,\phi;\theta',\phi')\cdot\overline{I}(\theta',\phi',z) \tag{1}$$

where $\overline{I}(\theta,\phi,z)$ is a 4×1 column vector denoting the Stokes parameters in direction (θ,ϕ),

$$\overline{I}(\theta,\phi,z) = \begin{bmatrix} I_v \\ I_h \\ U \\ V \end{bmatrix} \tag{2}$$

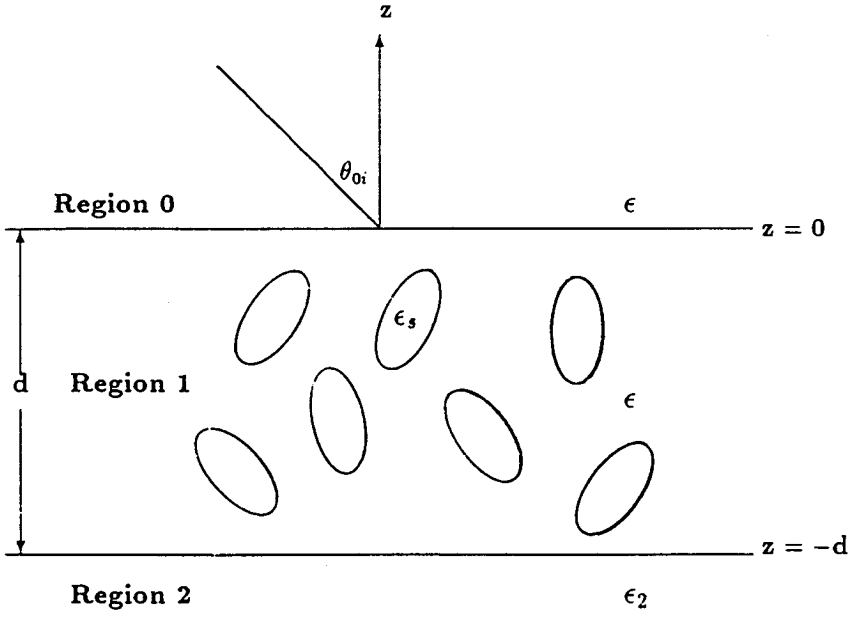

Figure 2.1 An incident plane wave impinging upon a layer of nonspherical particles overlying a homogeneous half space of permittivity ϵ_2.

In (2) $I_v = \langle |E_v|^2 \rangle / \eta$, $I_h = \langle |E_h|^2 \rangle / \eta$, $U = 2Re\langle E_v E_h^* \rangle / \eta$, and $V = 2Im\langle E_v E_h^* \rangle / \eta$, where the angular bracket $\langle\ \rangle$ denotes ensemble averaging. Subscripts v and h denote vertical and horizontal polarization respectively, and E_v, E_h denote the vertical and horizontal polarized components of the electric field respectively. In (1), $\overline{\overline{\kappa_e}}(\theta, \phi)$ is a 4×4 extinction matrix in direction (θ, ϕ) that is generally non-diagonal and direction dependent. The extinction matrix not only describes the extinction rates, but also contains the propagation constant difference between the vertical and horizontal polarized waves. In (1), $\overline{\overline{P}}(\theta, \phi; \theta', \phi')$ is the 4×4 phase matrix denoting scattering from direction (θ', ϕ') into direction (θ, ϕ). The elements of the extinction and phase matrices are expressed entirely in terms of the scattering function amplitudes that are averaged over size and orientation distributions of the nonspherical particles. For a single particle, the 2×2 scattering function matrix

from direction (θ', ϕ') into direction (θ, ϕ) is

$$\begin{bmatrix} f_{vv}(\theta,\phi;\theta',\phi') & f_{vh}(\theta,\phi;\theta',\phi') \\ f_{hv}(\theta,\phi;\theta',\phi') & f_{hh}(\theta,\phi;\theta',\phi') \end{bmatrix} \tag{3}$$

The extinction matrix can be expressed in terms of the forward scattering amplitudes [11]

$$\overline{\overline{\kappa_e}}(\theta,\phi) = \frac{2\pi n_o}{k} \begin{bmatrix} 2Im\langle f_{vv}\rangle & 0 \\ 0 & 2Im\langle f_{hh}\rangle \\ 2Im\langle f_{hv}\rangle & 2Im\langle f_{vh}\rangle \\ 2Re\langle f_{hv}\rangle & -2Re\langle f_{vh}\rangle \end{bmatrix}$$

$$\begin{bmatrix} Im\langle f_{vh}\rangle & -Re\langle f_{vh}\rangle \\ Im\langle f_{hv}\rangle & Re\langle f_{hv}\rangle \\ Im\langle f_{vv}+f_{hh}\rangle & Re\langle f_{vv}-f_{hh}\rangle \\ Re\langle f_{hh}-f_{vv}\rangle & Im\langle f_{vv}+f_{hh}\rangle \end{bmatrix} \tag{4}$$

where n_o is the number of particles per unit volume and all the $f_{j\ell}$, j, $\ell = v, h$ are forward scattering amplitudes. Explicitly, $f_{j\ell}$ is $f_{j\ell}(\theta,\phi;\theta,\phi)$ denoting scattering from (θ,ϕ) of polarization ℓ into the forward direction (θ,ϕ) of polarization j. In (4), the angular bracket $< >$ denotes averaging over orientation and size distributions of the particles. For example, for ellipsoids with semi-axes a, b, c and orientation Eulerian angles α, β, γ, the averaging for any g is performed as follows

$$\langle g\rangle = \int da \int db \int dc \int d\alpha \int d\beta \int d\gamma\, p(a,b,c,\alpha,\beta,\gamma)\, g \tag{5}$$

where $p(a,b,c,\alpha,\beta,\gamma)$ is the probability density function for the quantities a, b, c, α, β, and γ.

In terms of the scattering function amplitudes, the phase matrix $\overline{\overline{P}}(\theta,\phi;\theta',\phi')$ is [11]

$$\overline{\overline{P}}(\theta,\phi;\theta',\phi') = n_0 \begin{bmatrix} \langle|f_{vv}|^2\rangle & \langle|f_{vh}|^2\rangle \\ \langle|f_{hv}|^2\rangle & \langle|f_{hh}|^2\rangle \\ 2Re\langle f_{vv}f_{hv}^*\rangle & 2Re\langle f_{vh}f_{hh}^*\rangle \\ 2Im\langle f_{vv}f_{hv}^*\rangle & 2Im\langle f_{vh}f_{hh}^*\rangle \end{bmatrix}$$

$$\begin{bmatrix} Re\langle f_{vv}f_{vh}^*\rangle & -Im\langle f_{vv}f_{vh}^*\rangle \\ Re\langle f_{hv}f_{hh}^*\rangle & -Im\langle f_{hv}f_{hh}^*\rangle \\ Re\langle f_{vv}f_{hh}^*+f_{vh}f_{hv}^*\rangle & -Im\langle f_{vv}f_{hh}^*-f_{vh}f_{hv}^*\rangle \\ Im\langle f_{vv}f_{hh}^*+f_{vh}f_{hv}^*\rangle & Re\langle f_{vv}f_{hh}^*-f_{vh}f_{hv}^*\rangle \end{bmatrix} \tag{6}$$

where n_o is the number of particles per unit volume. In (6), all the $f_{j\ell}$, j, $\ell = v, h$ are bistatic scattering amplitudes. Explicitly, $f_{j\ell}$ is $f_{j\ell}(\theta, \phi; \theta', \phi')$ denoting scattering from a general direction (θ', ϕ') of polarization ℓ into direction (θ, ϕ) of polarization j.

In (1), we can distinguish between upward going Stokes vector $\overline{I}(\theta, \phi, z)$ and downward going Stokes vector $\overline{I}(\pi - \theta, \phi, z)$ with $0 \leq \theta \leq \pi/2$ and $0 \leq \phi \leq 2\pi$. The boundary conditions for the vector radiative transfer equation are as follows. At $z = 0$,

$$\overline{I}(\pi - \theta, \phi, z = 0) = \overline{I}_o \delta(\cos\theta - \cos\theta_o)\delta(\phi - \phi_o) \tag{7}$$

and at $z = -d$

$$\overline{I}(\theta, \phi, z = -d) = \overline{\overline{R}}(\theta) \cdot \overline{I}(\pi - \theta, \phi, z = -d) \tag{8}$$

for $0 \leq \theta \leq \pi/2$. In (8), $\overline{I}_o = [I_{vo}, I_{ho}, U_o, V_o]$ is the incident Stokes vector, $\overline{\overline{R}}(\theta)$ is the 4×4 reflectivity matrix for the interface separating between region 1 and region 2 and is given by

$$\overline{\overline{R}}(\theta) = \begin{bmatrix} |R_v(\theta)|^2 & 0 & 0 & 0 \\ 0 & |R_h(\theta)|^2 & 0 & 0 \\ 0 & 0 & Re(R_v(\theta)R_h^*(\theta)) & -Im(R_v(\theta)R_h^*(\theta)) \\ 0 & 0 & Im(R_v(\theta)R_h^*(\theta)) & Re(R_v(\theta)R_h^*(\theta)) \end{bmatrix} \tag{9}$$

where $R_v(\theta)$ and $R_h(\theta)$ are the Fresnel reflection coefficients for vertically and horizontally polarized waves.

$$R_v(\theta) = \frac{\epsilon_2 \cos\theta - \epsilon[\epsilon_2/\epsilon - \sin^2\theta]^{1/2}}{\epsilon_2 \cos\theta + \epsilon[\epsilon_2/\epsilon - \sin^2\theta]^{1/2}} \tag{10}$$

$$R_h(\theta) = \frac{\cos\theta - [\epsilon_2/\epsilon - \sin^2\theta]^{1/2}}{\cos\theta + [\epsilon_2/\epsilon - \sin^2\theta]^{1/2}} \tag{11}$$

Given the vector radiative transfer equation (1) and the boundary conditions in (7) and (8), the solutions for $\overline{I}(\theta, \phi, z)$ for $0 \leq \theta \leq \pi$ can be calculated either numerically or iteratively. Once that is solved, the overall scattered Stokes vector in direction (θ_s, ϕ_s) that is observed by the receiver is

$$\overline{I}_s(\theta_s, \phi_s) = \overline{I}(\theta_s, \phi_s, z = 0) \tag{12}$$

for $0 \leq \theta_s \leq \pi/2$, $0 \leq \phi_s \leq 2\pi$.

Since the vector radiative transfer equation is linear, $\bar{I}_s = [I_{vs}, I_{hs}, U_s, V_s]$ is proportional to $\bar{I}_o$ with the coupling represented by the 4×4 Mueller matrix $\bar{\bar{M}}(\theta_s, \phi_s; \pi - \theta_o, \phi_o)$ [9] as follows

$$\bar{I}_s(\theta_s, \phi_s) = \bar{\bar{M}}(\theta_s, \phi_s; \pi - \theta_o, \phi_o) \cdot \bar{I}_o \tag{13}$$

We note that the Mueller matrix as calculated here is an ensemble averaged quantity due to the ensemble averaged nature of transport theory. In actual experiment, the Mueller matrix is measured as a function of time and the results are then time-averaged. Thus by solving the vector radiative transfer equation of (1) subject to the boundary conditions (7) and (8), the Mueller matrix can be calculated. In this paper, we shall illustrate the results for backscattering direction with $\theta_s = \theta_o$ and $\phi_s = \pi + \phi_o$. The following polarimetric signatures are of particular interest.

The phase difference between vv and hh waves ϕ_{vh} is defined by

$$\phi_{vh} = \tan^{-1}\left(\frac{M_{43} - M_{34}}{M_{33} + M_{44}}\right) \tag{14}$$

where M_{ij} is the ij element of $\bar{\bar{M}}$.

For a completely polarized incident wave, with ellipticity angle χ, $-45° \leq \chi \leq 45°$ and orientation angle ψ, $0 \leq \psi \leq 180°$, the incident Stokes vector with unit total intensity is defined by

$$\bar{I}_o = \begin{bmatrix} (1 - \cos 2\chi \cos 2\psi)/2 \\ (1 + \cos 2\chi \cos 2\psi)/2 \\ -\cos 2\chi \sin 2\psi \\ \sin 2\chi \end{bmatrix} \tag{15}$$

This definition is a result of assuming an incident wave in the $\hat{z}'$ direction with incident field $\bar{E}_i = \hat{x}' E_{x'} + \hat{y}' E_{y'}$ and letting $E_{x'} = E_{h_i}$ and $E_{y'} = -E_{v_i}$. Thus the notation of the Stokes parameters is as in reference 11. However the $\hat{x}'$ direction is taken to be horizontal polarized while the $\hat{y}'$ direction is in the negative vertical polarization direction. The orientation angle ψ and ellipticity angle χ is defined with respect to $\hat{x}'$ and $\hat{y}'$. The normalized co-polarized received power in backscattering is that the receiving antenna polarization is the same as transmitting antenna polarization.

$$P_n = \frac{1}{2}(2I_{vs}I_{vo} + 2I_{hs}I_{ho} - U_sU_o + V_sV_o)$$

$$=\frac{I_{vs}}{2}(1-\cos 2\chi\cos 2\psi)+\frac{I_{hs}}{2}(1+\cos 2\chi\cos 2\psi)$$
$$+\frac{U_s}{2}\cos 2\chi\sin 2\psi+\frac{V_s}{2}\sin 2\chi \tag{16}$$

The backscattering co-polarization coefficient is

$$\sigma = 4\pi\cos\theta_o P_n \tag{17}$$

For depolarization, we consider polarization that is orthogonal to the incident polarization. The backscattering depolarization coefficient is defined as

$$\sigma_d = 4\pi\cos\theta_o\left[\frac{I_{vs}}{2}(1+\cos 2\chi\cos 2\psi)+\frac{I_{hs}}{2}(1-\cos 2\chi\cos 2\psi)\right.$$
$$\left.-\frac{U_s}{2}\cos 2\chi\sin 2\psi-\frac{V_s}{2}\sin 2\chi\right]$$
$$=4\pi\cos\theta_o(I_{vs}+I_{hs}-P_n) \tag{18}$$

The degree of polarization for the scattered Stokes vector is

$$m_s=\frac{(Q_s^2+U_s^2+V_s^2)^{1/2}}{I_s} \tag{19}$$

where $Q_s = I_{vs} - I_{hs}$ and $I_s = I_{vs} + I_{hs}$.

b. Extinction Matrix and Eigenvalues and Eigenmatrix of Coherent Propagation

The extinction matrix in terms of the forward scattering amplitudes is expressed in equation (4). The following points are important with regard to the extinction matrix and its calculation.

(a) The forward scattering amplitudes in the extinction matrix is to be averaged over orientation and size distributions with averaging as indicated in equation (5).

(b) The extinction matrix is derived from Foldy's approximation [11, p.138–140 and p.458–461]. Thus it is consistent with Foldy's integral equation for sparse concentration of particles.

(c) The extinction matrix is a generalization of the optical theorem for a sparse concentration of independent scatterers.

(d) In order to make use of the forward scattering amplitudes $f_{j\ell}(\theta, \phi; \theta, \phi)$ to calculate the extinction matrix, it is important that $f_{j\ell}(\theta, \phi; \theta, \phi)$ has to be evaluated to sufficient accuracy. Since the extinction matrix elements are in terms of both the real part and the imaginary part of the forward scattering amplitudes, the rule of thumb is to calculate $f_{j\ell}(\theta, \phi; \theta, \phi)$ up to the leading term of the real part and the leading term of the imaginary part. For example, the usual formula for scattering amplitude for Rayleigh scattering by dielectric sphere is not accurate enough to be used in the extinction matrix. In that case, it is easily shown that for real ϵ_s, $Imf_{vv} = Imf_{hh} = 0$. Thus to apply the results to the extinction matrix a more accurate formula for $f_{j\ell}(\theta, \phi; \theta, \phi)$ is required. For Mie scattering, exact solution for $f_{j\ell}(\theta, \phi; \theta, \phi)$ is available and can be directly used in calculating the extinction matrix. For general nonspherical particle when scattering amplitudes are usually calculated approximately, this point is particularly important.

(e) Although called extinction matrix, the extinction matrix contains the phase difference between the vertical and horizontal polarized components. This is evident by noting that the real parts of the forward scattering amplitude are also used in the extinction matrix. The 34 and 43 elements of the extinction matrix are particularly important in this regard.

(f) The extinction matrix represents coherent wave propagation in direction (θ, ϕ) with two characteristic waves with two corresponding complex characteristic propagation constants. These are generally dependent on direction (θ, ϕ). There are also two characteristic polarizations which can be neither vertical nor horizontal polarized waves. In the special case that $f_{vh}(\theta, \phi; \theta, \phi) = f_{hv}(\theta, \phi; \theta, \phi) = 0$, the vertical and horizontal polarization can be the characteristic polarizations. For the general case, the two characteristic propagation constants are

$$K_1 = k + \frac{\pi}{k}\left[n_o\langle f_{vv}(\theta, \phi; \theta, \phi)\rangle + n_o\langle f_{hh}(\theta, \phi; \theta, \phi)\rangle + R\right] \quad (20)$$

$$K_2 = k + \frac{\pi}{k}\left[n_o\langle f_{vv}(\theta, \phi; \theta, \phi)\rangle + n_o\langle f_{hh}(\theta, \phi; \theta, \phi)\rangle - R\right] \quad (21)$$

where

$$R = n_o\Big\{\left[\langle f_{vv}(\theta, \phi; \theta, \phi)\rangle - \langle f_{hh}(\theta, \phi; \theta, \phi)\rangle\right]^2 + 4\langle f_{hv}(\theta, \phi; \theta, \phi)\rangle\langle f_{vh}(\theta, \phi; \theta, \phi)\rangle\Big\}^{1/2} \quad (22)$$

where the sign of square root in (21) is chosen such that

$$\text{sgn } Re(R) = \text{sgn } [\langle f_{vv} \rangle - \langle f_{hh} \rangle] \tag{23}$$

The sign convention ensures that when $f_{hv}(\theta, \phi; \theta, \phi) = f_{vh}(\theta, \phi; \theta, \phi) = 0$ in (21), K_1 and K_2 will correspond to vertical and horizontal polarizations respectively.

(g) For coherent wave propagation, we consider the equation,

$$\frac{d\overline{I}^c}{ds} = -\overline{\overline{\kappa}}_e \, \overline{I}^c \tag{24}$$

for the coherent Stokes vector $\overline{I}^c$. By using solution $\overline{I}^c$ proportional to $exp(-\beta s)$, it readily follows from point (f) that there are four eigenvalues of β with

$$\beta_1 = 2ImK_1 \tag{25}$$
$$\beta_2 = 2ImK_2 \tag{26}$$
$$\beta_3 = i(K_1^* - K_2) \tag{27}$$
$$\beta_4 = i(K_2^* - K_1) \tag{28}$$

Note that β_1 and β_2 describe the extinction rates of the two characteristic polarizations. On the other hand β_3 and β_4 are complex conjugates of each other, and describe the phase and attenuation differences between the two characteristic polarizations. The corresponding eigenvectors can be represented in the eigenmatrix $\overline{\overline{E}}$ which obeys the equation

$$\overline{\overline{E}}\,\overline{\overline{\beta}} = \overline{\overline{\kappa}}_e \, \overline{\overline{E}} \tag{29}$$

where $\overline{\overline{\beta}}$ is a diagonal matrix with the ii element equal to β_i, $i = 1, 2, 3, 4$. The eigenmatrix $\overline{\overline{E}}$, in an unnormalized form, can be expressed as follows

$$\overline{\overline{E}}(\theta, \phi) = \begin{bmatrix} 1 & |b_2|^2 & b_2 & b_2^* \\ |b_1|^2 & 1 & b_1^* & b_1 \\ 2Reb_1 & 2Reb_2 & 1 + b_1^* b_2 & 1 + b_1 b_2^* \\ -2Imb_1 & 2Imb_2 & i(1 - b_1^* b_2) & -i(1 - b_1 b_2^*) \end{bmatrix} \tag{30}$$

where

$$b_1 = \frac{2n_o\langle f_{hv}(\theta,\phi;\theta,\phi)\rangle}{n_o\langle f_{vv}(\theta,\phi;\theta,\phi)\rangle - n_o\langle f_{hh}(\theta,\phi;\theta,\phi)\rangle + R} \tag{31}$$

$$b_2 = \frac{2n_o\langle f_{vh}(\theta,\phi;\theta,\phi)\rangle}{-n_o\langle f_{vv}(\theta,\phi;\theta,\phi)\rangle + n_o\langle f_{hh}(\theta,\phi;\theta,\phi)\rangle - R} \tag{32}$$

In equations (23) to (32), we have suppressed the (θ,ϕ) dependence of R, $\overline{\overline{E}}$, $\overline{\overline{\beta}}$, b_1, and b_2. The eigenmatrix is useful in formulating iterative solutions of the vector radiative transfer equation.

(h) For the special case that

$$\langle f_{hv}(\theta,\phi;\theta,\phi)\rangle = \langle f_{vh}(\theta,\phi;\theta,\phi)\rangle = 0 \tag{33}$$

(*e.g.* geophysical terrain that have statistical azimuthal symmetry), then the eigenvalues and eigenmatrices can be simplified as follows.

$$K_1 = k + \frac{2\pi}{k} n_o\langle f_{vv}(\theta,\phi;\theta,\phi)\rangle \tag{34}$$

$$K_2 = k + \frac{2\pi}{k} n_o\langle f_{hh}(\theta,\phi;\theta,\phi)\rangle \tag{35}$$

with β_1, β_2, β_3, and β_4, given by (25)–(28) and

$$\overline{\overline{E}} = \begin{bmatrix} 1 & 0 & 0 & 0 \\ 0 & 1 & 0 & 0 \\ 0 & 0 & 1 & 1 \\ 0 & 0 & i & -i \end{bmatrix} \tag{36}$$

In the Appendix, we list the extinction matrix elements for small spheroids that are uniformly oriented in Euler angle γ and are governed by a prescribed orientation distribution in Euler angle β.

c. Phase Matrix and Properties

In this section, we discuss some of the properties of the phase matrix that have important consequences for polarimetry.

It is first important to verify energy conservation for the vector radiative transfer equation especially for cases when the scattering amplitudes are calculated approximately. For the case when permittivity

of the particles ϵ_s is real, implying zero absorption, the following energy conservation relations must be obeyed [11, p.148]

$$\kappa_{e11}(\theta,\phi) = \int_0^{2\pi} d\phi' \int_0^{\pi} d\theta' \sin\theta' [P_{11}(\theta',\phi';\theta,\phi) + P_{21}(\theta',\phi';\theta,\phi)] \tag{37}$$

$$\kappa_{e22}(\theta,\phi) = \int_0^{2\pi} d\phi' \int_0^{\pi} d\theta' \sin\theta' [P_{12}(\theta',\phi';\theta,\phi) + P_{22}(\theta',\phi';\theta,\phi)] \tag{38}$$

$$\kappa_{e13}(\theta,\phi) + \kappa_{e23}(\theta,\phi) = \int_0^{2\pi} d\phi' \int_0^{\pi} d\theta' \sin\theta' [P_{13}(\theta',\phi';\theta,\phi) + P_{23}(\theta',\phi';\theta,\phi)] \tag{39}$$

$$\kappa_{e14}(\theta,\phi) + \kappa_{e24}(\theta,\phi) = \int_0^{2\pi} d\phi' \int_0^{\pi} d\theta' \sin\theta' [P_{14}(\theta',\phi';\theta,\phi) + P_{24}(\theta',\phi';\theta,\phi)] \tag{40}$$

Equations (37) and (38) represent extinction of the first two Stokes parameters while the equations (39) and (40) represent extinction of the third and fourth Stokes parameters.

Next we investigate the conditions on the phase matrix elements such that a single scattering of a completely polarized wave by a conglomeration of particles will also give a completely polarized wave. Let

$$\bar{I}_s(\theta_s,\phi_s) = \overline{\overline{P}}(\theta_s,\phi_s;\theta_i,\phi_i)\cdot\bar{I}_o \tag{41}$$

The degree of polarization of incident wave $\bar{I}_o$ is 1 so that

$$4I_{vo}I_{ho} = U_o^2 + V_o^2 \tag{42}$$

Then,

$$\begin{aligned} 4I_{vs}I_{hs} = 4(&P_{11}I_{vo} + P_{12}I_{ho} + P_{13}U_o + P_{14}V_o) \\ &(P_{21}I_{vo} + P_{22}I_{ho} + P_{23}U_o + P_{24}V_o) \end{aligned} \tag{43}$$

Making use of (41) and that $\bar{I}_o$ is completely polarized (equation (42)) gives

$$U_s^2 + V_s^2 = (P_{31}^2 + P_{41}^2)I_{vo}^2 + (P_{32}^2 + P_{42}^2)I_{ho}^2$$

$$
\begin{aligned}
&+2(P_{33}^2 + P_{44}^2 + P_{43}^2 + P_{34}^2)I_{vo}I_{ho} \\
&+2(P_{31}P_{33} + P_{41}P_{43})I_{vo}U_o + 2(P_{31}P_{34} + P_{41}P_{44})I_{vo}V_o \\
&+2(P_{32}P_{33} + P_{42}P_{43})I_{ho}U_o + 2(P_{32}P_{34} + P_{42}P_{44})I_{ho}V_o \\
&+\frac{1}{2}(P_{31}P_{32} + P_{41}P_{42} + P_{33}^2 - P_{44}^2 + P_{43}^2 - P_{34}^2)U_o^2 \\
&+\frac{1}{2}(P_{31}P_{32} + P_{41}P_{42} - P_{33}^2 + P_{44}^2 - P_{43}^2 + P_{34}^2)V_o^2 \\
&+2(P_{33}P_{34} + P_{43}P_{44})U_oV_o \qquad (44)
\end{aligned}
$$

Equating (43) and (44) gives the following conditions on the elements of the phase matrix such that a single scattering of a completely polarized wave by a conglomeration of scatterers or a random medium will still give a completely polarized wave

$$2(P_{11}P_{22} + P_{12}P_{21}) = P_{33}^2 + P_{44}^2 + P_{43}^2 + P_{34}^2 \qquad (45)$$

$$4P_{11}P_{21} = P_{31}^2 + P_{41}^2 \qquad (46)$$

$$4P_{12}P_{22} = P_{32}^2 + P_{42}^2 \qquad (47)$$

$$2(P_{11}P_{23} + P_{21}P_{13}) = P_{31}P_{33} + P_{41}P_{43} \qquad (48)$$

$$2(P_{11}P_{24} + P_{21}P_{14}) = P_{31}P_{34} + P_{41}P_{44} \qquad (49)$$

$$2(P_{12}P_{23} + P_{22}P_{13}) = P_{32}P_{33} + P_{42}P_{43} \qquad (50)$$

$$2(P_{12}P_{24} + P_{22}P_{14}) = P_{32}P_{34} + P_{42}P_{44} \qquad (51)$$

$$4P_{13}P_{23} = \frac{1}{2}(P_{31}P_{32} + P_{41}P_{42} + P_{33}^2 - P_{44}^2 + P_{43}^2 - P_{34}^2) \qquad (52)$$

$$4P_{14}P_{24} = \frac{1}{2}(P_{31}P_{32} + P_{41}P_{42} - P_{33}^2 + P_{44}^2 - P_{43}^2 + P_{34}^2) \qquad (53)$$

$$2(P_{14}P_{23} + P_{13}P_{24}) = P_{33}P_{34} + P_{43}P_{44} \qquad (54)$$

An example that the conditions (45)–(54) are obeyed is Rayleigh scattering by small spheres that can be governed by a drop size distribution [11,p.157]. In spite of the size distribution, the complex ratio of the scattered vertical polarized wave to that of the horizontal polarized wave is constant for all scatterers. Another example that the conditions

(45)–(54) are obeyed is the phase matrix as calculated for a random medium by using the Born approximation [11,p.164]. An example that (45)–(54) are not observed, as shown by the results in this chapter, is a conglomeration of spheroids that are randomly oriented. A sufficient condition that (45)–(54) are obeyed is that the scatterers are identical and are aligned.

d. First Order Solution of Mueller Matrix

By making use of the eigenmatrix of the extinction matrix, the vector radiative transfer equation (1) and the boundary conditions (7) and (8) can be cast into integral equations [11]. The first order iteration of the integral equations gives the first order solution of the Mueller matrix. The first order solution of the scattered wave in region 0 for the two layer medium of Fig. 2.1 contains four terms which can be physically interpreted as follows

(a) a reflection by the boundary at $z = -d$, followed by a single downward scattering by the particles and further followed by a reflection off the boundary at $z = -d$, which then proceeds upward to the receiver,

(b) a downward single scattering by the particles that is followed by a reflection off the boundary at $z = -d$.

(c) a reflection by the boundary that is followed by a single upward scattering by the particles, and

(d) a single upward scattering by the particles.

Between scattering by particles and reflection by boundary, the waves propagate with the coherent propagation constants as discussed in section 2.2b. Thus polarization phase differences are preserved in the theory. The first order solution of the Stokes vector is given in p.244 of reference 11. From that, one can readily calculate the Mueller matrix.

The first order solution of the Mueller matrix $\overline{\overline{M}}^{(1)}(\theta, \phi; \pi - \theta_o, \phi_o)$ is listed below

$$M_{\ell j}{}^{(1)}(\theta, \phi; \pi - \theta_o, \phi_o) =$$

$$\sum_{k,i} \sec\theta \left\{ \overline{\overline{E}}(\theta, \phi) \overline{\overline{D}} (-\beta(\theta, \phi) d \sec\theta) \overline{\overline{E}}^{-1}(\theta, \phi) \overline{\overline{R}}(\theta) \overline{\overline{E}}(\pi - \theta, \phi) \right\}_{\ell k}$$

$$\times \left\{ \overline{\overline{E}}^{-1}(\pi - \theta, \phi) \overline{\overline{P}}(\pi - \theta, \phi; \theta_o, \phi_o) \overline{\overline{E}}(\theta_o, \phi_o) \right\}_{ki}$$

$$
\begin{aligned}
&\times \frac{1-e^{-\beta_k(\pi-\theta,\phi)d\sec\theta-\beta_i(\theta_o,\phi_o)d\sec\theta_o}}{\beta_k(\pi-\theta,\phi)\sec\theta+\beta_i(\theta_o,\phi_o)\sec\theta_o}\left\{\overline{\overline{E}}^{-1}(\theta_o,\phi_o)\overline{\overline{R}}(\theta_o)\right.\\
&\left.\cdot\,\overline{\overline{E}}(\pi-\theta_o,\phi_o)\overline{\overline{D}}\left(-\beta(\pi-\theta_o,\phi_o)d\sec\theta_o\right)\overline{\overline{E}}^{-1}(\pi-\theta_o,\phi_o)\right\}_{ij}\\
&+\sum_{k,i}\sec\theta\left\{\overline{\overline{E}}(\theta,\phi)\overline{\overline{D}}\left(-\beta(\theta,\phi)d\sec\theta\right)\overline{\overline{E}}^{-1}(\theta,\phi)\overline{\overline{R}}(\theta)\overline{\overline{E}}(\pi-\theta,\phi)\right\}_{\ell k}\\
&\times\left\{\overline{\overline{E}}^{-1}(\pi-\theta,\phi)\overline{\overline{P}}(\pi-\theta,\phi;\pi-\theta_o,\phi_o)\overline{\overline{E}}(\pi-\theta_o,\phi_o)\right\}_{ki}\\
&\times\frac{e^{-\beta_k(\pi-\theta,\phi)d\sec\theta-\beta_i(\pi-\theta_o,\phi_o)d\sec\theta_o}}{\beta_i(\pi-\theta_o,\phi_o)\sec\theta_o-\beta_k(\pi-\theta,\phi)\sec\theta}\left\{\overline{\overline{E}}^{-1}(\pi-\theta_o,\phi_o)\right\}_{ij}\\
&+\sec\theta\sum_{k,i}\overline{\overline{E}}_{\ell k}(\theta,\phi)\left\{\overline{\overline{E}}^{-1}(\theta,\phi)\overline{\overline{P}}(\theta,\phi;\theta_o,\phi_o)\overline{\overline{E}}(\theta_o,\phi_o)\right\}_{ki}\\
&\times\frac{e^{-\beta_k(\theta,\phi)d\sec\theta-\beta_i(\theta_o,\phi_o)d\sec\theta_o}}{\beta_i(\theta_o,\phi_o)\sec\theta_o-\beta_k(\theta,\phi)\sec\theta}\left\{\overline{\overline{E}}^{-1}(\theta_o,\phi_o)\overline{\overline{R}}(\theta_o)\right.\\
&\left.\cdot\,\overline{\overline{E}}(\pi-\theta_o,\phi_o)\overline{\overline{D}}\left(-\beta(\pi-\theta_o,\phi_o)d\sec\theta_o\right)\overline{\overline{E}}^{-1}(\pi-\theta_o,\phi_o)\right\}_{ij}\\
&+\sec\theta\sum_{k,i}\overline{\overline{E}}_{\ell k}(\theta,\phi)\left\{\overline{\overline{E}}^{-1}(\theta,\phi)\overline{\overline{P}}(\theta,\phi;\pi-\theta_o,\phi_o)\overline{\overline{E}}(\pi-\theta_o,\phi_o)\right\}_{ki}\\
&\times\frac{1-e^{-\beta_k(\theta,\phi)d\sec\theta-\beta_i(\pi-\theta_o,\phi_o)d\sec\theta_o}}{\beta_k(\theta,\phi)\sec\theta+\beta_i(\pi-\theta_o,\phi_o)\sec\theta_o}\left\{\overline{\overline{E}}^{-1}(\pi-\theta_o,\phi_o)\right\}_{ij}
\end{aligned}
\tag{55}
$$

The four terms in (55) correspond respectively to the physical interpretations (a), (b), (c), and (d) above.

Our first order solution is different from the conventional single scattering solution. The conventional single scattering solution is usually regarded as a single volume scattering from the medium without considering the attenuation of the incident wave nor reflection by boundaries. The first order solution in (55) has four terms and includes the effects of boundary reflection. Also, the attenuation of incident wave is taken into account as exhibited by factors of the form $(\beta_k \sec\theta + \beta_i \sec\theta_o)^{-1}$ in equation (55). Because of the differences in propagation constants between polarizations, these factors contribute to interesting polarimetric signatures.

e. Second Order Solution of Mueller Matrix

The expression of the second order solution for a two layer medium is very complicated. In the following we give the expression for the case of half space with $d \to \infty$ in Fig. 2.1. The second order theory consists of the sum of the first order solution and the second order solution of the vector radiative transfer equation. The first and second order solutions correspond respectively to the first and second iterations of the integral equation.

$$M_{mj}(\theta,\phi;\pi-\theta_o,\phi_o) = M_{mj}^{(1)}(\theta,\phi;\pi-\theta_o,\phi_o) + M_{mj}^{(2)}(\theta,\phi;\pi-\theta_o,\phi_o) \tag{56}$$

with

$$M_{mj}^{(1)}(\theta,\phi;\pi-\theta_o,\phi_o) = \sum_{k,i} \cos\theta_o E_{mk}(\theta,\phi) \left\{ \overline{\overline{E}}^{-1}(\theta,\phi)\overline{\overline{P}}(\theta,\phi;\pi-\theta_o,\phi_o)\overline{\overline{E}}(\pi-\theta_o,\phi_o) \right\}_{ki} \times \frac{E_{ij}^{-1}(\pi-\theta_o,\phi_o)}{\beta_k(\theta,\phi)\cos\theta_o + \beta_i(\pi-\theta_o,\phi_o)\cos\theta_o} \tag{57}$$

$$\begin{aligned} M_{mj}^{(2)}(\theta,\phi;\pi-\theta_o,\phi_o) = & \sum_{n,k,i} E_{mn}(\theta,\phi) \frac{\cos\theta_o E_{ij}^{-1}(\pi-\theta_o,\phi_o)}{\beta_n(\theta,\phi)\cos\theta_o + \beta_i(\pi-\theta_o,\phi_o)\cos\theta_o} \\ & \times \int_0^{2\pi} d\phi' \int_0^{\pi/2} d\theta' \sin\theta' \left[\left\{ \overline{\overline{E}}^{-1}(\theta,\phi)\overline{\overline{P}}(\theta,\phi;\theta',\phi')\overline{\overline{E}}(\theta',\phi') \right\}_{nk} \right. \\ & \times \left\{ \overline{\overline{E}}^{-1}(\theta',\phi')\overline{\overline{P}}(\theta',\phi';\pi-\theta_o,\phi_o)\overline{\overline{E}}(\pi-\theta_o,\phi_o) \right\}_{ki} \\ & \times \frac{\cos\theta_o}{\beta_k(\theta',\phi')\cos\theta_o + \beta_i(\pi-\theta_o,\phi_o)\cos\theta'} \\ & + \left\{ \overline{\overline{E}}^{-1}(\theta,\phi)\overline{\overline{P}}(\theta,\phi;\pi-\theta',\phi')\overline{\overline{E}}(\pi-\theta',\phi') \right\}_{nk} \\ & \times \left\{ \overline{\overline{E}}^{-1}(\pi-\theta',\phi')\overline{\overline{P}}(\pi-\theta',\phi';\pi-\theta_o,\phi_o)\overline{\overline{E}}(\pi-\theta_o,\phi_o) \right\}_{ki} \\ & \left. \times \frac{\cos\theta}{\beta_n(\theta,\phi)\cos\theta' + \beta_k(\pi-\theta',\phi')\cos\theta} \right] \end{aligned} \tag{58}$$

f. Numerical Results of Radar Polarimetry

The formulation of vector radiative transfer theory in sections 2.2a to 2.2e is applicable to general nonspherical particles with arbitrary sizes and orientation distributions. In this section, we illustrate the numerical results of radar polarimetry of a layer of small spheroids overlying a homogeneous half-space. In the appendix, we list the extinction and phase matrix elements of spheroids that are uniformly oriented in Euler angle γ and are governed by orientation distribution in angle β.

In Figs. 2.2 to 2.5, we illustrate the numerical results when the orientation in β is uniform between β_1 and β_2. Hence the averaging is taken as follows:

$$\langle g \rangle = \frac{1}{\cos\beta_1 - \cos\beta_2} \int_{\beta_1}^{\beta_2} d\beta \sin\beta \, g \tag{59}$$

For the case of $\beta_1 = 0°$ and $\beta_2 \to 0°$, the spheroids are aligned with axis of symmetry in the z direction.

In Figs. 2.2(a), (b) and (c), we illustrate the results for aligned oblate spheroids. In Figs. 2.2(a), 2.2(b) and 2.2(c) the backscattering copolarization coefficient, depolarization coefficient and degree of polarization are plotted respectively as a function of ellipticity angle χ and polarization orientation angle ψ. The oblate spheroids are aligned. The layer thickness is optically thin. The parameters chosen for discrete scatterers and dielectric permittivity of the lower half space represent typical values of leaves in vegetation [4,32]. The case of $\chi = 0°$, $\psi = 90°$ represents incident vertical polarization and the case of $\chi = 0°$, $\psi = 0°$ represents incident horizontal polarization. Horizontal polarization produces larger return than vertical polarized waves while circular polarization produces negligible copolarization return. In Fig. 2.2(b), we note that the depolarization coefficient is largest for circular polarized incident waves. In Fig. 2.2(c), we plot the degree of polarization. The degree of polarization for the scattered wave is close to unity for all incident polarizations. This is because the particles are identical in sizes and orientation and the layer is optically thin so that under the single scattering approximation as discussed in section 2.2c, the phase matrix has the property of preserving the degree of polarization to be unity. In Figs. 2.3(a), (b) and (c), we illustrate the results for randomly oriented spheroids with $\beta_1 = 0°$ and $\beta_2 = 90°$. We note in Fig. 2.3(a) that the copolarization return has less variation than that of

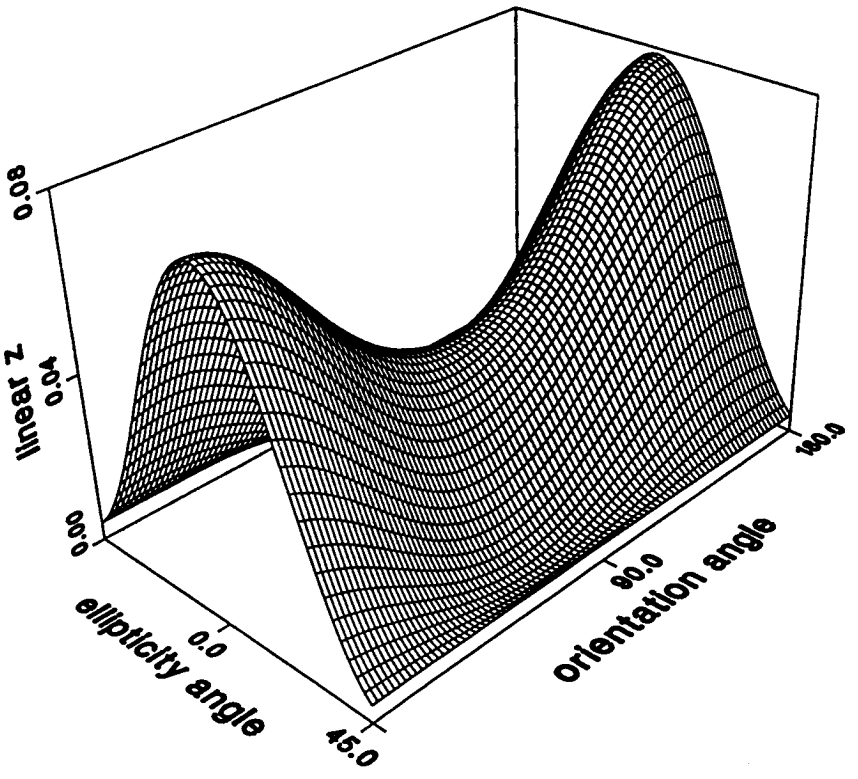

Figure 2.2a Polarization signatures based on first order theory as a function of ellipticity angle χ and polarization orientation angle ψ of a layer of aligned spheroids with *frequency* $= 1.225GHz$, $\epsilon_s = (6.5+i0.5)\epsilon_o$, $a = 2.5cm$, $c = 0.25cm$, *fractional volume* $= 0.0055$, $d = 2.5m$, $\epsilon_2 = (15+i2)\epsilon_o$, **and** $\theta_o = 35°$. **Orientation distribution is governed by** $\beta_1 = 0°$, **and** $\beta_2 \to 0°$. **(2a) copolarization coefficient** ($\sigma = 7.882 \times 10^{-2}$ **at** $\psi = 180°$, $\chi = 0°$).

Fig. 2.2(a). There is finite copolarization return for circular polarized waves and less difference between the returns of vertical and horizontal polarized incidence. The copolarization also exhibits a pedestal. Thus the results illustrate the effects of heterogeneity of scatterers because although the scatterers are identical in size and shape, they are oriented in different directions and thus have different scattering properties from the point of view of the transmitter. In Fig. 2.3(b), we illustrate the depolarization signature. In Fig. 2.3(c), the degree of polarization is plotted. We note that the degree of polarization is no

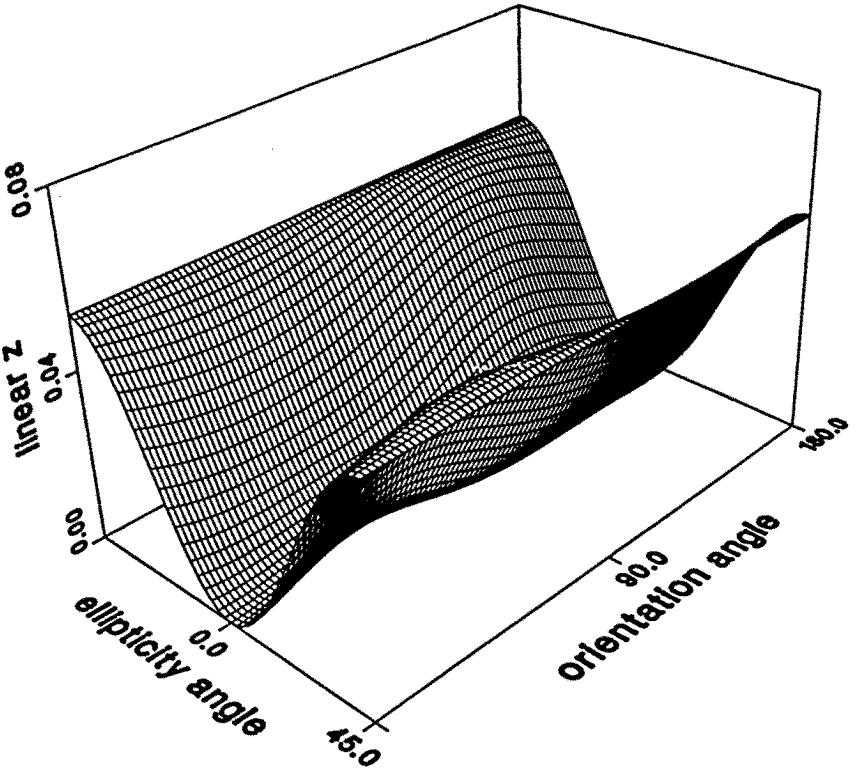

Figure 2.2b Depolarization coefficient ($\sigma_d = 5.245 \times 10^{-2}$ **at** $\psi = 180°$, $\chi = -45°$).

longer equal to unity as a result of averaging over the orientation of the spheroids. Comparison between Figs. 2.2(c) and 2.3(c) indicates that there is a big difference of degree of polarization between the case of aligned scatterers and randomly oriented scatterers.

In Fig. 2.4, the phase difference (14) between vv and hh waves are plotted as a function of β_2 with $\beta_1 = 0$. Two angles of incidence of 35° and 60° are considered. We note that there exists a finite phase difference for aligned scatterers. This is because, for aligned spheroids, there exist two effective propagation constants that are appreciably different. The phase difference is also larger for a larger angle of incidence. However, as β_2 increases representing an increase in the variance of orientation, the phase difference decreases which implies that the effective anisotropy of the medium decreases.

In Fig. 2.5, we plot the degree of polarization of the scattered

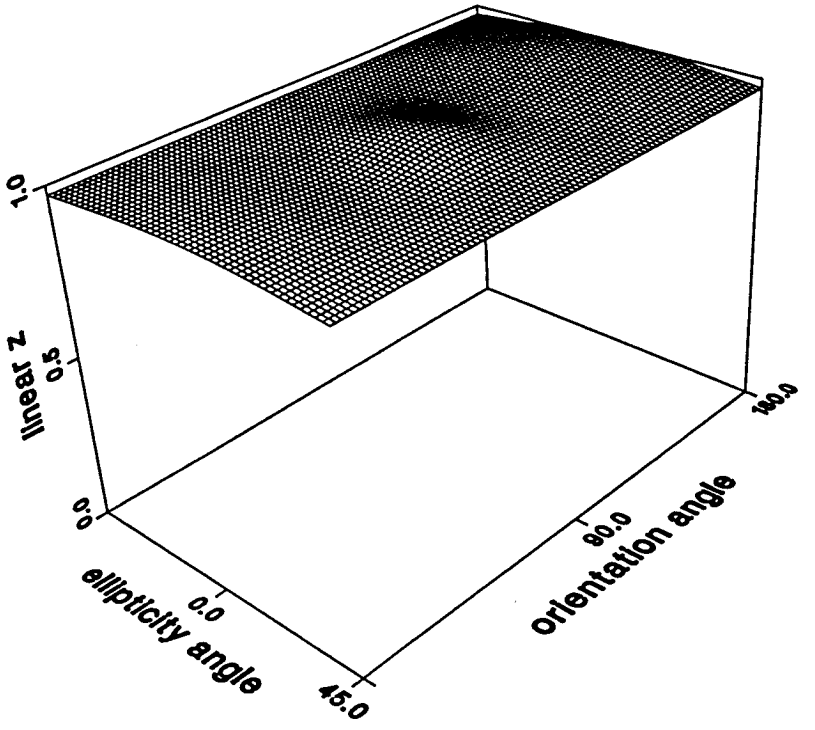

Figure 2.2c Degree of polarization.

wave for a left hand circular polarized incident wave as a function of β_2. We note that as β_2 increases, the degree of polarization decreases as a result of differences in scattering between different scatterers. We note that for the case of aligned scatterers, the degree of polarization is not equal to unity in spite of the fact that the scatterers are identical. This is because the first order solution is more than single scattering. It includes the difference in attenuation between the two polarizations as exhibited in a circular polarized incident wave.

In Figs. 2.6 and 2.7, we compare the results between first order theory and the second order theory for a half space medium with less lossy aligned scatterers. The degree of polarization is generally less than unity for both first order theory and second order theory because of the phase differences and attenuation rate difference between the two propagation constants. We note that multiple scattering effects as exhibited in Fig. 2.7 generally show less polarization contrast than first

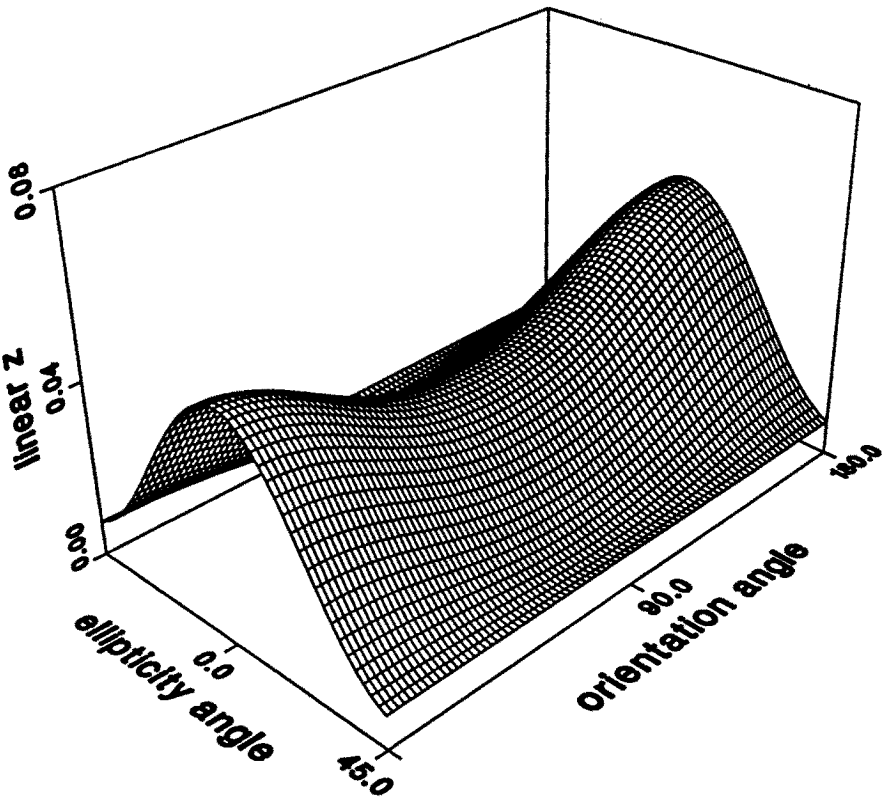

Figure 2.3a Polarization signatures based on first order theory as a function of ellipticity angle χ and polarization orientation angle ψ of a layer of randomly oriented spheroids with *frequency* $= 1.225GHz$, $\epsilon_s = (6.5+i0.5)\epsilon_o$, $a = 2.5cm$, $c = 0.25cm$, *fractional volume* $= 0.0055$, $d = 2.5m$, $\epsilon_2 = (15 + i2)\epsilon_o$, **and** $\theta_o = 35°$. **Orientation distribution is governed by** $\beta_1 = 0°$, **and** $\beta_2 = 90°$. **(3a) copolarization coefficient** ($\sigma = 5.161 \times 10^{-2}$ **at** $\psi = 180°$, $\chi = 0°$).

order scattering in Fig. 2.6.

2.3 Part II. Dense Media Radiative Transfer Theory

a. Effective Propagation Constants, Extinction Rates and Albedo for Dense Medium with Particle Size Distribution and Multiple Permittivities

To study the propagation and scattering of waves in dense me-

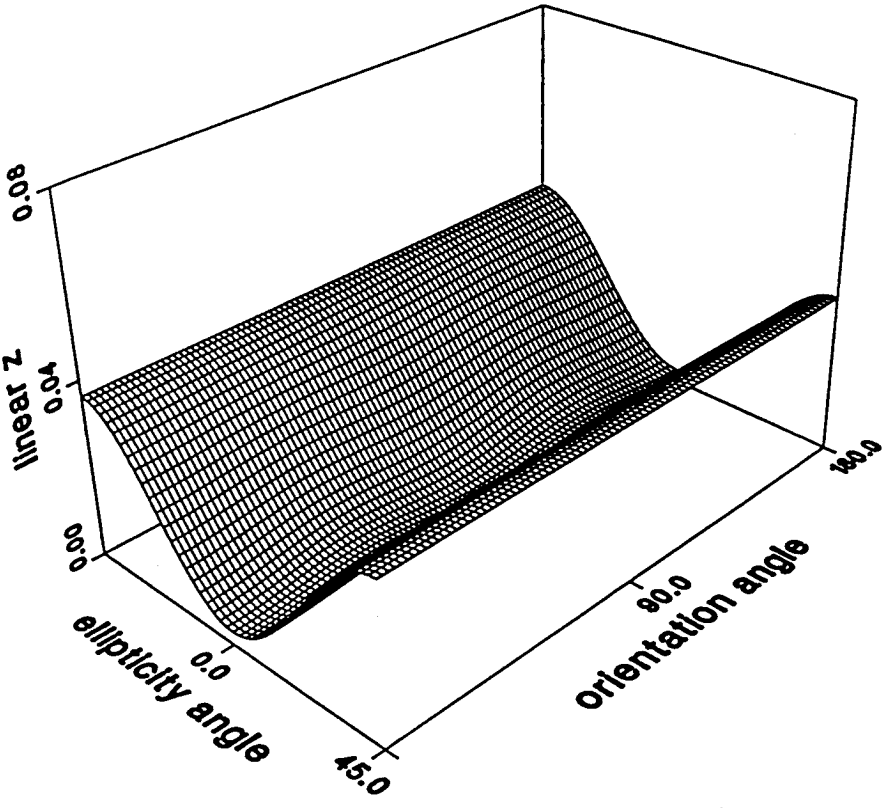

Figure 2.3b Depolarization coefficient ($\sigma_d = 3.646 \times 10^{-2}$ **at** $\psi = 180°$, $\chi = -45°$).

dia, we have derived dense medium radiative transfer equations from the Dyson's equation under the quasicrystalline approximation with coherent potential (QCA–CP) and the Bethe–Salpeter equation under the ladder approximation of correlated scatterers [11,18,19]. The energy conservation is satisfied exactly under the combination of these two approximations. The dense medium transfer equations take into account the correlated scattering effects and correct the deficiencies of the conventional theory. We have also extended our treatment of dense medium transfer theory to media consisting of multiple species of particles [20–22]. The multiple species refers to the fact that the medium is a mixture of particles with different sizes and permittivities. This is particularly important because particle sizes in geophysical terrain generally follow a size distribution and can also consist of different constituents. Three important quantities for this theory are the effective

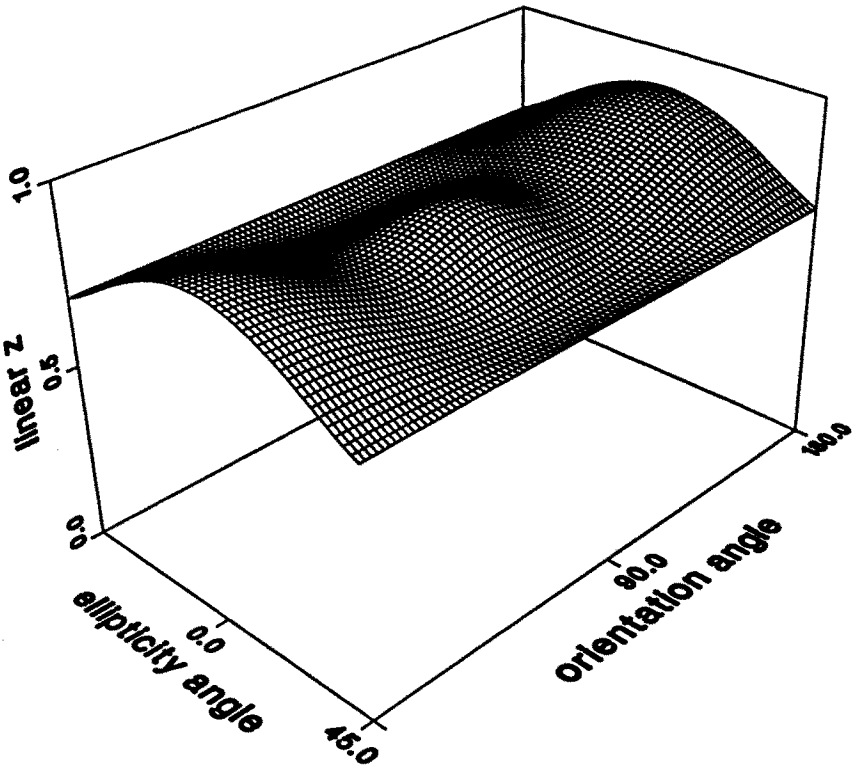

Figure 2.3c Degree of polarization.

propagation constant, extinction rate and albedo. They are computed from the input physical parameters of the model which are the background medium permittivity, the particle permittivities and their size distributions. The pair distribution functions for media with multiple species of particles are calculated by using the Percus-Yevick approximation [27–29] which are in good agreement with Monte Carlo and laboratory simulations [30,31].

Consider a medium with densely distributed particles with multiple sizes and permittivities. Let there be L species and let s_j, $s_j = 1, 2, \cdots, L$, be the species index. The volume fraction $f_{s_j} = 4\pi n_{s_j} a_{s_j}^3/3$ of the s_j species can be appreciable and the wavenumber $k_{s_j} = \omega\sqrt{\mu\epsilon_{s_j}}$ of particles of species s_j can be substantially different from the background wavenumber k. The quantities a_{s_j} and n_{s_j} are respectively the radius and the number of particles per unit volume of species s_j. Hence, the effective propagation constant K of the medium may be

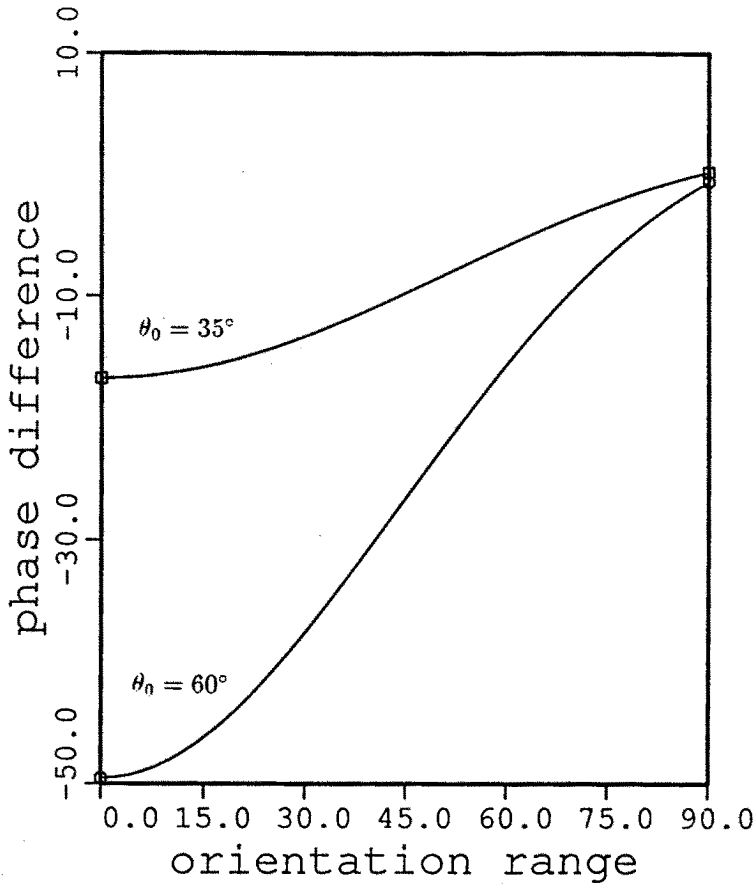

Figure 2.4 Phase difference ϕ_{vh} in degrees (equation (14)) based on first order theory of a layer of spheroids as a function of orientation distribution β_2 in degrees for $\beta_1 = 0°$. At $\beta_2 \to 0°$ spheroids are aligned. Two angles of incidence $\theta_o = 35°$ and $\theta_o = 60°$ are considered. Other parameters are *frequency* $= 1.225GHz$, $\epsilon_s = (6.5 + i0.5)\epsilon_o$, $a = 2.5cm$, $c = 0.25cm$, *fractional volume* $= 0.0055$, $d = 2.5m$, and $\epsilon_2 = (15 + i2)\epsilon_o$.

very different from k of the background medium.

The propagation of coherent wave in a medium is characterized by the effective propagation constant. The effective propagation constant K is generally complex with the imaginary part accounting for the attenuation of the coherent wave due to both absorption and scattering.

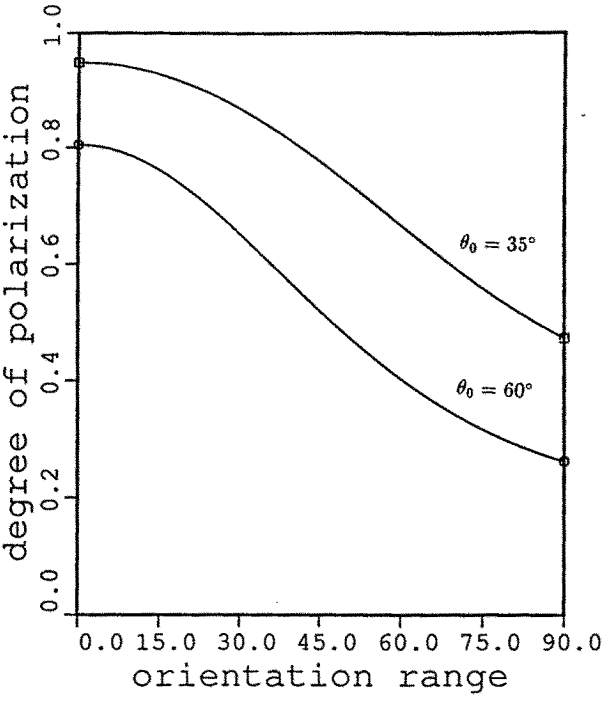

Figure 2.5 Degree of polarization based on first order theory of a layer of spheroids as a function of orientation distribution β_2 in degrees for $\beta_1 = 0°$. At $\beta_2 \to 0°$ spheroids are aligned. Two angles of incidence $\theta_o = 35°$ and $\theta_o = 60°$ are considered. Incident wave is left hand circularly polarized. Other parameters are as follows. *frequency* $= 1.225GHz$, $\epsilon_s = (6.5+i0.5)\epsilon_o$, $a = 2.5cm$, $c = 0.25cm$, *fractional volume* $= 0.0055$, $d = 2.5m$, and $\epsilon_2 = (15 + i2)\epsilon_o$.

Generally, $K' \equiv Re(K) \gg Im(K) \equiv K''$. For the case of small spherical particles, $ka_{s_j} \ll 1$, the effective propagation constant K under the quasicrystalline approximation with coherent potential is governed by the relation [20,21]

$$\begin{aligned} K^2 \approx & K'^2 + i2K'K'' \\ = & k^2 + \frac{3K_o^2}{D(K_o)} \sum_{s_\ell=1}^{L} f_{s_\ell} y_{s_\ell}(K_o) \times \left\{ 1 + i\frac{2K_o^3}{3D(K_o)} \left[a_{s_\ell}^3 y_{s_\ell}(K_o) \right.\right. \\ & \left.\left. + \sum_{s_j=1}^{L} y_{s_j}(K_o) a_{s_j}^3 n_{s_j} 8\pi^3 H_{s_j s_\ell}(p=0) \right] \right\} \end{aligned} \tag{60}$$

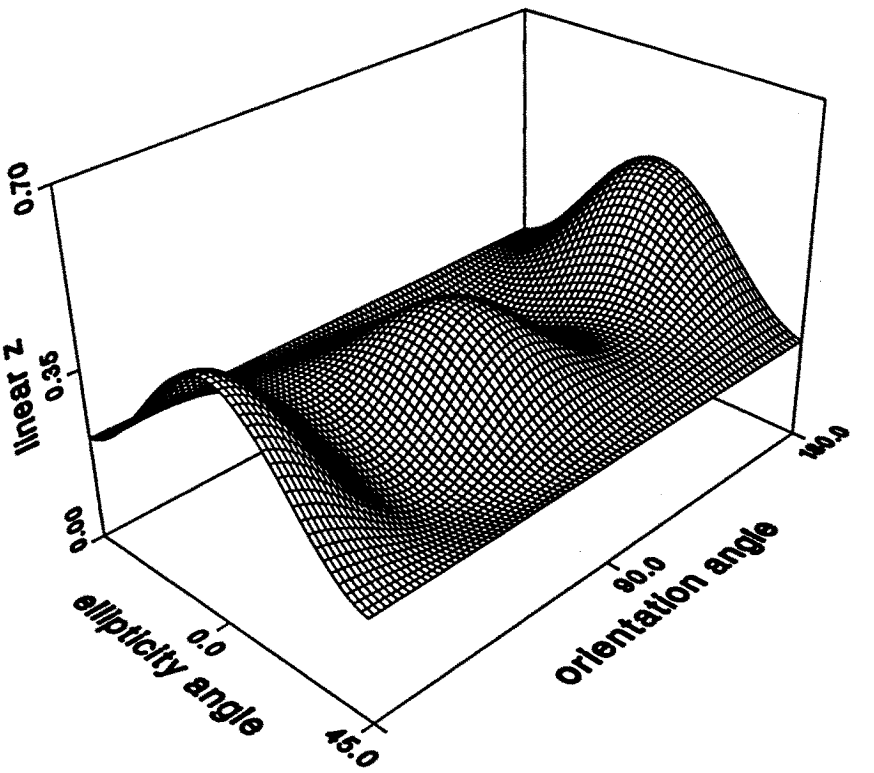

Figure 2.6a Polarization signatures of a half space of aligned spheroids based on first order theory as a function of ellipticity angle χ and polarization orientation angle ψ. Other parameters are as follows. *frequency* $= 1.225GHz$, $\epsilon_s = (6.5+i0.05)\epsilon_o$, $a = 2.5cm$, $c = 0.25cm$, *fractional volume* $= 0.0055$, $d = 2.5m$, $\epsilon_2 = (15+i2)\epsilon_o$, **and** $\theta_o = 35°$. **Orientation distribution is** $\beta_1 = 0°$, **and** $\beta_2 \to 0°$. **(6a) copolarization coefficient** ($\sigma = 0.479$ **at** $\psi = 180°$, $\chi = 0°$).

where K_o^2 satisfies the following equation

$$K_o^2 = k^2 + \frac{3K_o^2}{D(K_o)} \sum_{s_l=1}^{L} f_{s_l} y_{s_l}(K_o) \tag{61}$$

which is also equivalent to the dielectric mixing formula [20,21]

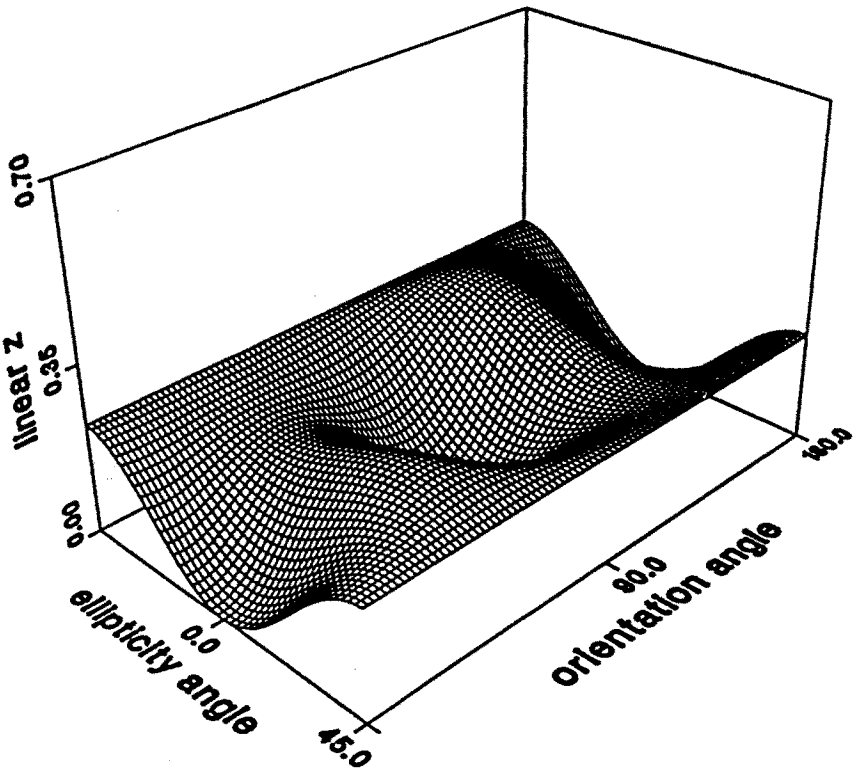

Figure 2.6b Depolarization coefficient ($\sigma_d = 0.226$ **at** $\psi = 180°$, $\chi = -45°$).

$$\epsilon_{eff} = \epsilon + \frac{3\epsilon_{eff} \sum_{s_j=1}^{L} f_{s_j} \dfrac{\epsilon_{s_j} - \epsilon}{3\epsilon_{eff} + \epsilon_{s_j} - \epsilon}}{1 - \sum_{s_j=1}^{L} f_{s_j} \dfrac{\epsilon_{s_j} - \epsilon}{3\epsilon_{eff} + \epsilon_{s_j} - \epsilon}} \tag{62}$$

The effective permittivity ϵ_{eff} is given by $\epsilon_{eff}/\epsilon = K^2/k^2$. Physically, K_o indicates the propagation constant when particle sizes are so small that the scattering attenuation rate can be ignored. In the above equations (60) and (61), $y_{s_j}(K_o)$ and $D(K_o)$ are functions of K_o defined

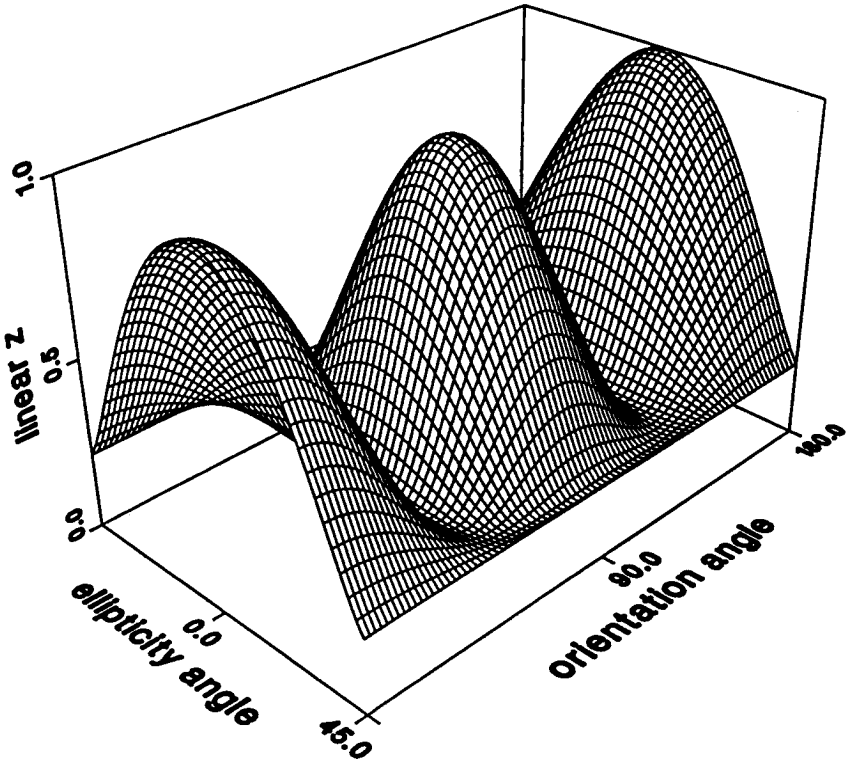

Figure 2.6c Degree of polarization.

as

$$y_{s_j}(K_o) = \frac{k_{s_j}^2 - k^2}{3K_o^2 + (k_{s_j}^2 - k^2)} \tag{63}$$

$$D(K_o) = 1 - \sum_{s_j=1}^{L} f_{s_j} y_{s_j}(K_o) \tag{64}$$

The quantities $H_{s_j s_l}(\overline{p})$ in (60) are related to the Fourier transforms of pair distribution functions by

$$H_{s_j s_l}(\overline{p}) = \frac{1}{(2\pi)^3} \int_{-\infty}^{\infty} d\overline{r}\; e^{i\overline{p}\cdot\overline{r}} h_{s_j s_l}(\overline{r}) \tag{65}$$

and

$$h_{s_j s_l}(\overline{r}) = g_{s_j s_l}(\overline{r}) - 1 \tag{66}$$

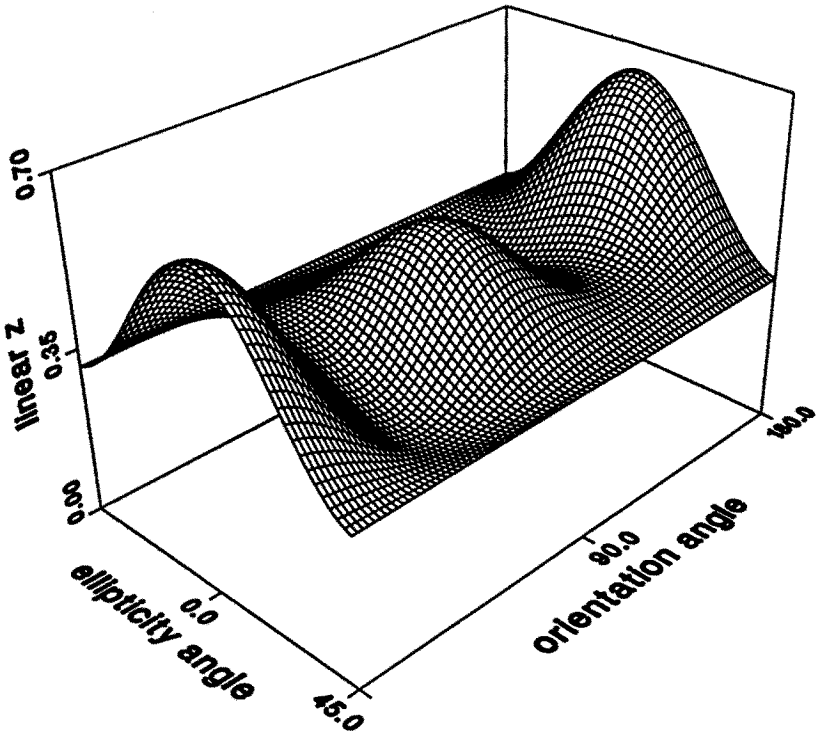

Figure 2.7a Polarization signatures of a half space of aligned spheroids based on second order theory as a function of ellipticity angle χ and polarization orientation angle ψ. Other parameters are as follows. *frequency* $= 1.225GHz$, $\epsilon_s = (6.5 + i0.05)\epsilon_o$, $a = 2.5cm$, $c = 0.25cm$, *fractional volume* $= 0.0055$, $d = 2.5m$, $\epsilon_2 = (15 + i2)\epsilon_o$, **and** $\theta_o = 35°$. **Orientation distribution is** $\beta_1 = 0°$, **and** $\beta_2 \to 0°$. **(7a) copolarization coefficient** ($\sigma = 0.649$ **at** $\psi = 180°$, $\chi = 0°$).

where $g_{s_j s_\ell}(\bar{r})$ is the pair distribution function of two particles of species s_j and s_ℓ separated by $\bar{r}$. The multiple species pair functions can be computed by the Percus–Yevick approximation [20,21,27–29]. The total correlation function $h_{s_j s_\ell}(\bar{r})$ is generally non-zero over a range of a few particle diameters.

The Fourier transforms $H_{s_i s_j}(p = 0)$ in (60) can be calculated by solving the $L \times L$ matrix equation

$$\overline{\overline{\tilde{H}}}(p = 0) = \overline{\overline{\tilde{C}}}(p = 0) + \overline{\overline{\tilde{C}}}(p = 0)\overline{\overline{\tilde{H}}}(p = 0) \tag{67}$$

where the matrix elements $\tilde{H}_{s_i s_j}(p = 0)$ and $H_{s_i s_j}(p = 0)$ are related

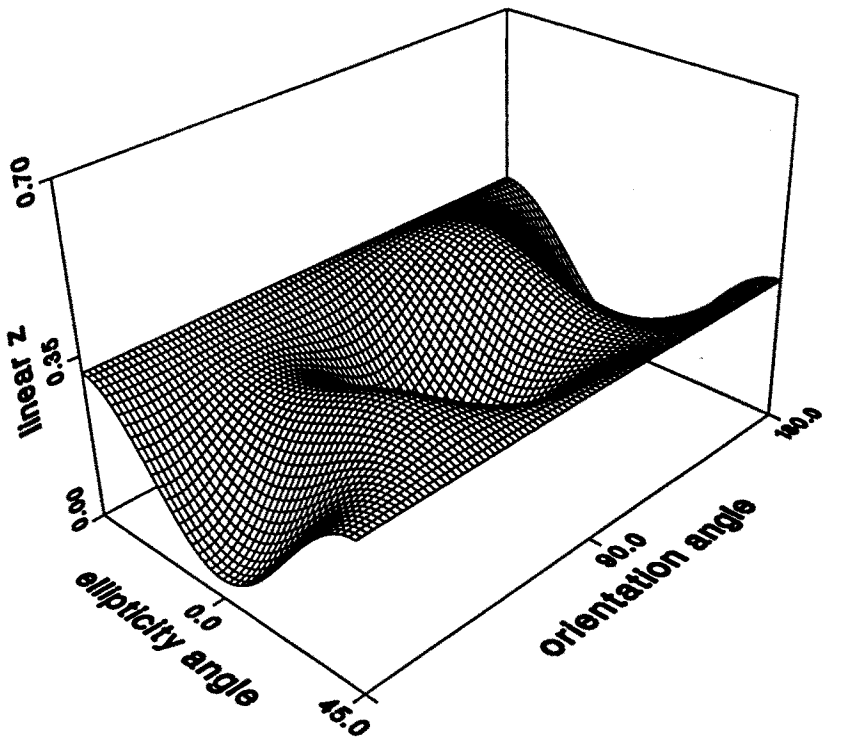

Figure 2.7b Depolarization coefficient ($\sigma_d = 0.314$ at $\psi = 180°$, $\chi = -45°$).

by

$$H_{s_i s_j}(p=0) = \frac{\widetilde{H}_{s_i s_j}(p=0)}{(2\pi)^3 \sqrt{n_{s_i} n_{s_j}}} \tag{68}$$

Equation (67) is the matrix form of the multicomponent Ornstein–Zernike relation [27,29] at $p = 0$. The matrix $\overline{\overline{\widetilde{C}}}(p=0)$ in (67) is defined by a similar equation to (68) for the direct correlation function $c_{s_i s_j}(r)$ [29], and $\widetilde{C}_{s_i s_j}(p=0)$ takes the following form

$$\widetilde{C}_{s_i s_j}(p=0) =$$
$$-\frac{\pi}{6}\sqrt{n_{s_i} n_{s_j}} \left[\frac{(R_{s_i} + R_{s_j})^3}{1-\xi_3} + \frac{3R_{s_i}R_{s_j}\xi_2(R_{s_i}^2 + R_{s_j}^2)}{(1-\xi_3)^2} \right.$$
$$\left. + \frac{3R_{s_i}^2 R_{s_j}^2 \xi_1 (R_{s_i} + R_{s_j}) + 9R_{s_i}^2 R_{s_j}^2 \xi_2 + R_{s_i}^3 R_{s_j}^3 \xi_0}{(1-\xi_3)^2} \right.$$

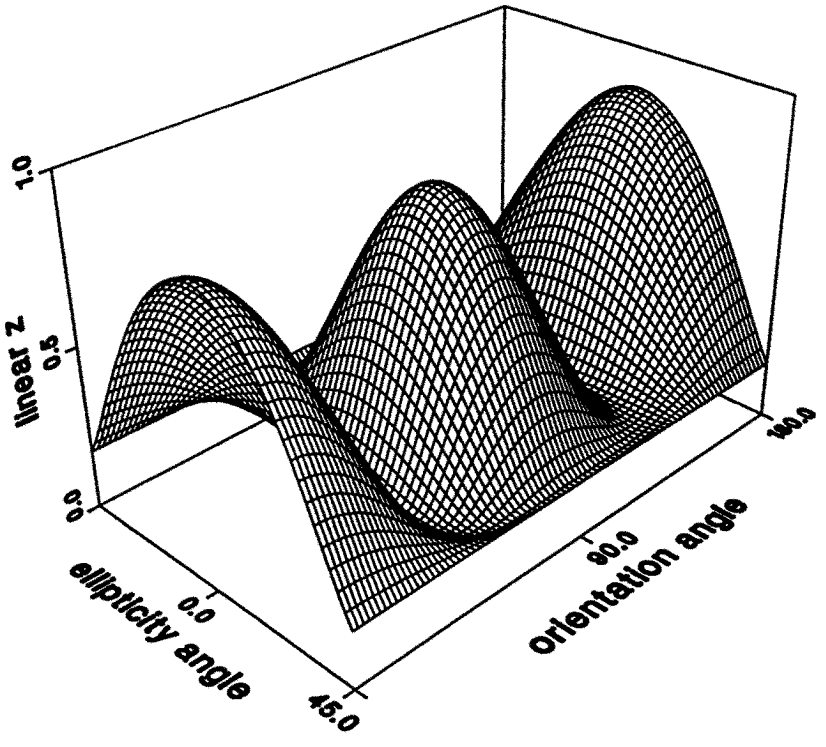

Figure 2.7c Degree of polarization.

$$+\frac{9R_{s_i}^2R_{s_j}^2\xi_2^2(R_{s_i}+R_{s_j})+6R_{s_i}^3R_{s_j}^3\xi_1\xi_2}{(1-\xi_3)^3}+\frac{9R_{s_i}^3R_{s_j}^3\xi_2^3}{(1-\xi_3)^4}\Bigg] \tag{69}$$

where $R_{s_is_j}$ is the sum of radii a_{s_i} and a_{s_j},

$$R_{s_is_j}=a_{s_i}+a_{s_j} \tag{70}$$

and the parameters ξ_m are defined by

$$\xi_m=\frac{\pi}{6}\sum_{s_j=1}^{L}n_{s_j}(2a_{s_j})^m \tag{71}$$

for $m=0,1,2,3$. Thus, given the species radii a_{s_j} and number densities n_{s_j}, $\widetilde{C}_{s_is_j}(p=0)$ can be computed from equations (69)–(71). Then, the elements $H_{s_is_j}(p=0)$, for $s_i, s_j=1,2,\cdots,L$, are calculated by solving the matrix equation (67) and making use of the relation (68).

The extinction rate and albedo are calculated as follows. For a medium with multiple species of particles, the extinction rate κ_e is

$$\kappa_e = 2K'' \tag{72}$$

where $K'' = Im(K)$. The albedo $\tilde{\omega}$ for the multiple species medium is given by [11,22]

$$\tilde{\omega} = \frac{2|K_o|^4}{\kappa_e |D(K_o)|^2} \sum_{s_l=1}^{L} f_{s_l} y_{s_l}(K_o) \left\{ a_{s_l}^3 y_{s_l}^*(K_o) + \sum_{s_j=1}^{L} n_{s_j} a_{s_j}^3 y_{s_j}^*(K_o) 8\pi^3 H_{s_j s_l}(p=0) \right\} \tag{73}$$

where K_o is given in (61). For the case of medium with lossless particles, it follows that K_o, $y_{s_j}(K_o)$ and $D(K_o)$ are all real and $K_o = K'$. The extinction rate κ_e becomes

$$\kappa_e = \frac{2K_o^4}{D(K_o)^2} \sum_{s_l=1}^{L} f_{s_l} y_{s_l}(K_o) \left\{ a_{s_l}^3 y_{s_l}(K_o) + \sum_{s_j=1}^{L} n_{s_j} a_{s_j}^3 y_{s_j}(K_o) 8\pi^3 H_{s_j s_l}(p=0) \right\} \tag{74}$$

In this case, the extinction is totally due to scattering and albedo $\tilde{\omega}$ is equal to unity. It is noted that both the attenuation rate and albedo are expressed in terms of the physical parameters of the medium: sizes, concentrations, and the dielectric properties of the particles. This allows us to study the electromagnetic responses of the medium directly through the target characteristics.

In the studies of remote sensing of geophysical terrain, very often the ground truth data are given in terms of a histogram of particle size distribution. The multiple species model is applicable to a medium with size distribution. A general expression for particle size distribution is the modified gamma distribution [11,34,35]

$$n(a) = K_1 a^P \exp\left(-K_2 a^Q\right) \tag{75}$$

where a is the size of particle and $n(a)da$ gives the number of particles per unit volume having sizes between a and $a + da$.

The modified gamma distribution defined in (75) is a four-parameter distribution function. The four constants K_1, P, K_2, and Q are positive and real. The behavior of this distribution function for small size is governed by the power law of a^P, and for large a, $\exp\left(-K_2 a^Q\right)$ contains the dropoff at large particle size. The normalizing factor K_1 is mainly dependent on the total fractional volume f_{tot} occupied by particles per unit volume. This is obtained by multiplying $n(a)$ by $(4/3)\pi a^3$ and integrating over the entire range of size (from 0 to ∞)

$$f_{tot} = \frac{4\pi}{3}\frac{K_1}{Q}K_2^{-\frac{P+4}{Q}}\Gamma\left(\frac{P+4}{Q}\right) \tag{76}$$

The parameter K_2 is related to the mode size a_c at which $n(a_c)$ is a maximum in the distribution, where a_c can be found by setting the derivative of (75) with respect to a equal to zero.

$$a_c = \left(\frac{P}{K_2 Q}\right)^{\frac{1}{Q}} \tag{77}$$

One may construct a great variety of specific distributions based on the general formula (75). Usually, the constants P and Q can be fitted empirically to the slopes of an experimentally obtained particle size distribution.

For a medium with particle size distribution, we can discretize the continuous size distribution into a histogram of L different sizes to incorporate the results shown above. Given the sets of L discretized sizes a_{s_j} and number densities n_{s_j}, the process of computing the effective propagation constant K, the extinction rate κ_e and the albedo $\tilde{\omega}$ is summarized as follows.

Step 1. Obtain the corresponding fractional volume f_{s_j} for each of the L species by making use of the relation $f_{s_j} = 4\pi n_{s_j} a_{s_j}^3/3$.

Step 2. Compute the effective propagation constant K_o by solving (61) and the functions $y_{s_j}(K_o)$ and $D(K_o)$ from (63) and (64). Note that (61) is a nonlinear equation of K_o because both $y_{s_j}(K_o)$ and $D(K_o)$ depend on K_o. We can cast equation (61) into a polynomial equation of K_o^2, generally, the coefficients of this polynomial are complex. The complex roots are readily solved by using some FORTRAN subroutines (e.g. IMSL). Actually, there is only one solution which has the correct physical meaning of effective propagation constant. Substitute the correct solution of K_o into (63) and (64), $y_{s_j}(K_o)$ and $D(K_o)$ can be calculated.

Step 3. The Fourier transform quantities $H_{s_i s_j}(p = 0)$ in (60) are calculated by using equations (67)–(71). The elements $\widetilde{C}_{s_i s_j}(p = 0)$ are firstly evaluated from (69)–(71), the matrix equation (67) is next solved and $H_{s_i s_j}(p = 0)$ are computed by using (68).

Step 4. Once $H_{s_i s_j}(p = 0)$, $y_{s_j}(K_o)$ and $D(K_o)$ are obtained, we can proceed to calculate the effective propagation constant K by using (60).

Step 5. The extinction rate κ_e and albedo $\tilde{\omega}$ are calculated by using equations (72) and (73) respectively.

In this manner, the effective propagation constant K under QCA–CP can be calculated and is numerically illustrated in Fig. 2.8.

In Fig. 2.8, we illustrate the normalized attenuation rate κ_e/k as a function of the total fractional volume of particles. The permittivity chosen for particles is $3.2\epsilon_o$. The results are also compared for two sets of size distribution parameters, $P = 6$, $Q = 4$, $f_{tot} = 0.2$, and $a_c = 0.1cm$, and $0.125cm$. The size distributions have been discretized into thirty different sizes and the pair functions are also calculated. We note that the attenuation rate first increases with f_{tot}, then rises to a peak and decreases when f_{tot} further increases. This indicates that the medium appears more homogeneous as f_{tot} further increases beyond a certain value. It also indicates that the medium with more large particles (larger a_c) can have significantly larger scattering attenuation rates.

b. Vector Radiative Transfer Theory for Dense Media

Consider the same geometric configuration as Fig. 2.1 with region 1 now occupied by densely distributed multiple species of spherical particles (Fig. 2.9). The slab is of thickness d (region 1) and lies above a homogeneous medium with permittivity of ϵ_2 (region 2). A plane wave of angular frequency ω is incident from region 0 upon the two-layer medium in direction $(\pi - \theta_o, \phi_o)$. The propagation and scattering of waves in region 1 is governed by the dense medium radiative transfer equation [11,18,22]. For $0 \leq \theta \leq \pi$ and $0 \leq \phi \leq 2\pi$

$$\cos\theta \frac{d}{dz}\bar{I}(\theta,\phi,z) = -\kappa_e \bar{I}(\theta,\phi,z) + \int_0^{2\pi} d\phi' \int_0^{\pi} d\theta' \sin\theta' \bar{\bar{P}}(\theta,\phi;\theta',\phi') \cdot \bar{I}(\theta',\phi',z) \tag{78}$$

where $\bar{I}(\theta,\phi,z)$ is the Stokes vector in the direction (θ,ϕ). The ex-

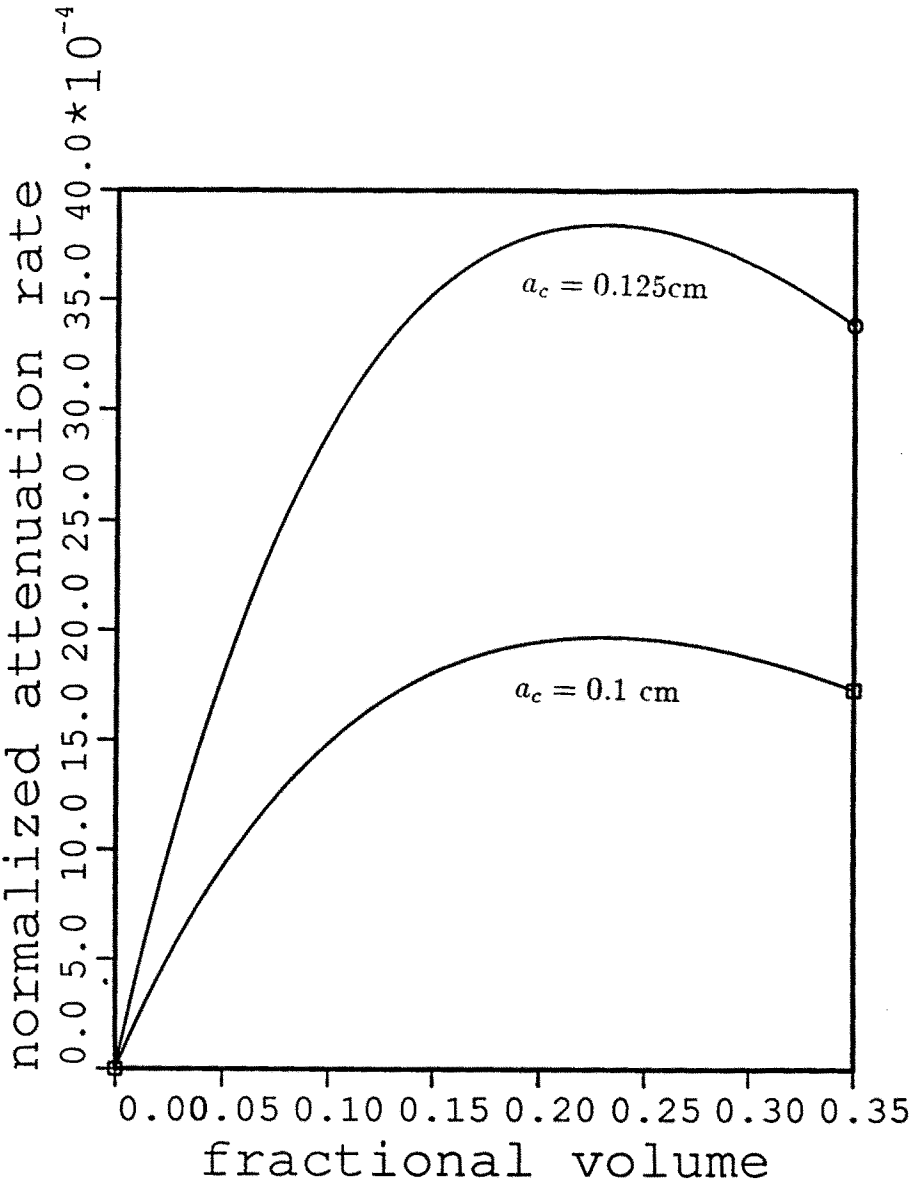

Figure 2.8 Normalized attenuation rate κ_e/k as a function of f_{tot}, for (1) $a_c = 0.1cm$ and (2) $a_c = 0.125cm$, with $P = 6$, $Q = 4$, $\epsilon_s = 3.2\epsilon_o$ and $frequency = 17GHz$.

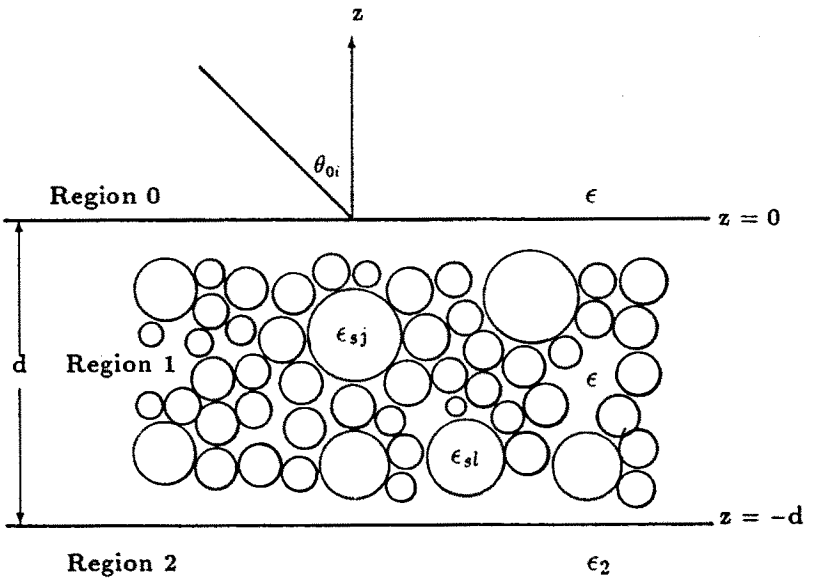

Figure 2.9 An incident plane wave impinging upon a layer of densely distributed spherical particles overlying a homogeneous half space of permittivity ϵ_2.

tinction rate κ_e and albedo $\tilde{\omega}$ are given by (72) and (73), respectively. The dense medium radiative transfer equation (76) resembles that of conventional radiative transfer equation [23,34] except that the expression for κ_e and $\tilde{\omega}$ are different because of correlated scattering and the effective propagation constant K is also taken into account [11,18,22].

The elements of the 4×4 phase matrix $\overline{\overline{P}}(\theta,\phi;\theta',\phi')$ are [11, p.155–158]

$$P_{11} = \frac{3\kappa_e\tilde{\omega}}{8\pi}[\sin\theta\sin\theta' + \cos\theta\cos\theta'\cos(\phi-\phi')]^2 \tag{79}$$

$$P_{12} = \frac{3\kappa_e\tilde{\omega}}{8\pi}\cos^2\theta\sin^2(\phi-\phi') \tag{80}$$

$$P_{13} = \frac{3\kappa_e\tilde{\omega}}{8\pi}[\sin\theta\sin\theta' + \cos\theta\cos\theta'\cos(\phi-\phi')]\cos\theta\sin(\phi-\phi') \tag{81}$$

$$P_{21} = \frac{3\kappa_e\tilde{\omega}}{8\pi}\cos^2\theta'\sin^2(\phi-\phi') \tag{82}$$

$$P_{22} = \frac{3\kappa_e\tilde{\omega}}{8\pi}\cos^2(\phi-\phi') \tag{83}$$

$$P_{23} = -\frac{3\kappa_e\tilde{\omega}}{8\pi}\cos\theta'\sin(\phi-\phi')\cos(\phi-\phi') \tag{84}$$

$$P_{31} = -\frac{3\kappa_e\tilde{\omega}}{4\pi}\cos\theta'\sin(\phi-\phi')[\sin\theta\sin\theta'+\cos\theta\cos\theta'\cos(\phi-\phi')] \tag{85}$$

$$P_{32} = \frac{3\kappa_e\tilde{\omega}}{4\pi}\cos\theta\cos(\phi-\phi')\sin(\phi-\phi') \tag{86}$$

$$P_{33} = \frac{3\kappa_e\tilde{\omega}}{8\pi}[\sin\theta\sin\theta'\cos(\phi-\phi')+\cos\theta\cos\theta'\cos 2(\phi-\phi')] \tag{87}$$

$$P_{44} = \frac{3\kappa_e\tilde{\omega}}{8\pi}[\sin\theta\sin\theta'\cos(\phi-\phi')+\cos\theta\cos\theta'] \tag{88}$$

$$P_{14} = P_{24} = P_{34} = P_{41} = P_{42} = P_{43} = 0 \tag{89}$$

The phase matrix is identical to the Rayleigh phase matrix of the conventional radiative transfer theory [11]. This is because of the small particle assumption and that the pair distribution functions are only correlated for the range of a few diameters which are less than a wavelength.

In the original derivation of the dense medium radiative transfer equations, the electric field has been decomposed into a coherent part and an incoherent part. To obtain (78), the coherent and incoherent intensities are added together to form the total Stokes vector. At the boundary between region 0 and region 1, the Snell's law can be applied so that the transmitted angle of the coherent wave in region 1 is $\theta = \sin^{-1}(k\sin\theta_o/K')$ where $K' = Re(K)$ is the real part of the effective propagation constant in region 1. The boundary conditions for the Stokes vector are, at $z = 0$ for $0 \le \theta \le \pi/2$, [11,33]

$$\bar{I}(\pi-\theta,\phi,z=0) = \bar{\bar{T}}_{01}(\theta_o)\cdot\bar{I}_o(\pi-\theta_o,\phi_o)+\bar{\bar{R}}_{10}(\theta)\cdot\bar{I}(\theta,\phi,z=0) \tag{90}$$

and at $z = -d$ for $0 \le \theta \le \pi/2$,

$$\bar{I}(\theta,\phi,z=-d) = \bar{\bar{R}}_{12}(\theta)\cdot\bar{I}(\pi-\theta,\phi,z=-d) \tag{91}$$

where $\bar{I}_o(\pi-\theta_o,\phi_o)$ is the incident Stokes vector in direction $(\pi-\theta_o,\phi_o)$,

$$\bar{I}_o(\pi-\theta,\phi) = \bar{I}_o\delta(\cos\theta-\cos\theta_o)\,\delta(\phi-\phi_o) \tag{92}$$

with $\overline{I}_o = [I_{vo}, I_{ho}, U_o, V_o]$. In equations (90)–(91), $\overline{I}(\theta, \phi, z)$ and $\overline{I}(\pi - \theta, \phi, z)$ represent respectively the upward and downward going Stokes vectors in region 1. The transmissivity matrix $\overline{\overline{T}}_{01}(\theta_o)$ represents the coupling from region 0 to region 1 for the Stokes vector, and the reflectivity matrix $\overline{\overline{R}}_{10}(\theta)$ represents the coupling from upward-going intensity into downward-going intensity at the interface of region 0 and region 1. Similarly, $\overline{\overline{R}}_{12}(\theta)$ represents the reflectivity matrix of Stokes vector at the boundary $z = -d$.

The reflectivity and transmissivity matrices in boundary conditions (90)–(91) follow also from the ladder approximation of Bethe-Salpeter equation [11]. They are basically those of Fresnel relations using ϵ for region 0, the effective permittivity ϵ_1 for region 1 and ϵ_2 for region 2. The 4×4 coupling matrices $\overline{\overline{R}}_{pq}(\theta)$ and $\overline{\overline{T}}_{01}(\theta_o)$ in (90)–(91) take the forms, for $p, q = 0, 1, 2$, [11,33]

$$\overline{\overline{R}}_{pq}(\theta) = \begin{bmatrix} |R_{vpq}(\theta)|^2 & 0 \\ 0 & |R_{hpq}(\theta)|^2 \\ 0 & 0 \\ 0 & 0 \end{bmatrix}$$

$$\begin{matrix} 0 & 0 \\ 0 & 0 \\ Re(R_{vpq}(\theta)R^*_{hpq}(\theta)) & -Im(R_{vpq}(\theta)R^*_{hpq}(\theta)) \\ Im(R_{vpq}(\theta)R^*_{hpq}(\theta)) & Re(R_{vpq}(\theta)R^*_{hpq}(\theta)) \end{matrix} \Bigg] \tag{93}$$

and

$$\overline{\overline{T}}_{01}(\theta_o) = \frac{\epsilon_1}{\epsilon_o} \begin{bmatrix} t_v(\theta_o) & 0 \\ 0 & t_h(\theta_o) \\ 0 & 0 \\ 0 & 0 \end{bmatrix}$$

$$\begin{matrix} 0 & 0 \\ 0 & 0 \\ \beta(\theta_o)Re(T_v(\theta_o)T^*_h(\theta_o)) & -\beta(\theta_o)Im(T_v(\theta_o)T^*_h(\theta_o)) \\ \beta(\theta_o)Im(T_v(\theta_o)T^*_h(\theta_o)) & \beta(\theta_o)Re(T_v(\theta_o)T^*_h(\theta_o)) \end{matrix} \Bigg] \tag{94}$$

where $R_{vpq}(\theta)$ and $R_{hpq}(\theta)$ are respectively the Fresnel reflection coefficients for vertically and horizontally polarized waves,

$$R_{vpq}(\theta) = \frac{\epsilon_q \cos\theta - \epsilon_p[\epsilon_q/\epsilon_p - \sin^2\theta]^{1/2}}{\epsilon_q \cos\theta + \epsilon_p[\epsilon_q/\epsilon_p - \sin^2\theta]^{1/2}} \tag{95}$$

$$R_{hpq}(\theta) = \frac{\cos\theta - [\epsilon_q/\epsilon_p - \sin^2\theta]^{1/2}}{\cos\theta + [\epsilon_q/\epsilon_p - \sin^2\theta]^{1/2}} \tag{96}$$

and

$$t_v(\theta_o) = 1 - |R_{v01}(\theta_o)|^2 \tag{97}$$

$$t_h(\theta_o) = 1 - |R_{h01}(\theta_o)|^2 \tag{98}$$

$$T_v(\theta_o) = 1 + R_{v01}(\theta_o) \tag{99}$$

$$T_h(\theta_o) = 1 + R_{h01}(\theta_o) \tag{100}$$

$$\beta(\theta_o) = \frac{\sqrt{1 - (\epsilon_o/\epsilon_1)\sin^2\theta_o}}{\cos\theta_o} \tag{101}$$

for θ_o less than the critical angle, otherwise $T_v(\theta_o) = T_h(\theta_o) = 0$. The effective dielectric constant ϵ_1 in region 1 is given as

$$\epsilon_1 = \frac{\epsilon_o K'^2}{k^2} \tag{102}$$

Once the dense medium radiative transfer equations are solved subject to the boundary conditions, the scattered Stokes vector in the direction (θ_s, ϕ_s) in region 0 is obtained as

$$\overline{I}_s(\theta_s, \phi_s, z = 0) = \overline{\overline{T}}_{10}(\theta_s) \cdot \overline{I}(\theta_s, \phi_s, z = 0) \tag{103}$$

where $\overline{I}_s = [I_{vs}, I_{hs}, U_s, V_s]$ and $\overline{\overline{T}}_{10}(\theta_s)$ is the transmissivity matrix of the Stokes vector from region 1 to region 0 and is the expression of (94) with interchange of 1 and 0 and the angles in the two regions related by Snell's Law. The Mueller matrix $\overline{\overline{M}}$ which couples the scattered Stokes vector $\overline{I}_s$ and incident Stokes vector $\overline{I}_o$, is calculated by the equation

$$\overline{I}_s(\theta_s, \phi_s) = \overline{\overline{M}}(\theta_s, \phi_s; \pi - \theta_o, \phi_o) \cdot \overline{I}_o \tag{104}$$

with $\overline{I}_s(\theta_s, \phi_s) = \overline{I}_s(\theta_s, \phi_s, z = 0)$ as in (13).

The bistatic coefficient $\gamma_{\beta\alpha}(\theta_s, \phi_s; \theta_o, \phi_o)$ and the backscattering coefficient $\sigma_{\beta\alpha}(\theta_o)$, at $\theta_s = \theta_o$ and $\phi_s = \pi + \phi_o$, are defined as [11]

$$\gamma_{\beta\alpha}(\theta_s, \phi_s; \theta_o, \phi_o) = 4\pi \frac{\cos\theta_s I_{\beta s}(\theta_s, \phi_s)}{\cos\theta_o I_{\alpha o}} \tag{105}$$

$$\sigma_{\beta\alpha}(\theta_o) = \cos\theta_o \gamma_{\beta\alpha}(\theta_o, \pi + \phi_o; \theta_o, \phi_o) \tag{106}$$

where $\alpha, \beta = v$ or h.

c. *Multiple Scattering Solutions*

The dense medium radiative transfer equation has a similar form to that of the conventional radiative transfer equation. Thus, the same numerical technique, discrete ordinate-eigenanalysis method [11,34], can be used to solve for the dense medium radiative transfer equations including Stokes vectors and Mueller matrices. All orders of multiple scattering within radiative transfer theory are included in this numerical solution.

We first expand the Stokes vector $\bar{I}(\theta, \phi, z)$ and the phase matrix $\bar{\bar{P}}(\theta, \phi; \theta', \phi')$ into Fourier series in the azimuthal direction to eliminate the ϕ-dependence from the dense medium radiative transfer equation (78). They are [10,11]

$$\bar{I}(\theta, \phi, z) = \sum_{m=0}^{\infty} \left[\bar{I}^{mc}(\theta, z) \cos m(\phi - \phi_i) + \bar{I}^{ms}(\theta, z) \sin m(\phi - \phi_i)\right] \tag{107}$$

and

$$\bar{\bar{P}}(\theta, \phi; \theta', \phi') = \sum_{m=0}^{M} \left[\bar{\bar{P}}^{mc}(\theta, \theta') \cos m(\phi - \phi') + \bar{\bar{P}}^{ms}(\theta, \theta') \sin m(\phi - \phi')\right] \tag{108}$$

where superscripts mc and ms indicates respectively the mth order harmonics of cosine and sine dependences in the azimuthal directions. We note that for Rayleigh scatterers the phase matrices $\bar{\bar{P}}^{mc}(\theta, \theta')$ and $\bar{\bar{P}}^{ms}(\theta, \theta')$ become zero as $m \geq 3$ and the upper limit in (108) is $M = 2$ for Rayleigh scatterers [10,11]. Thus, the phase matrices $\bar{\bar{P}}^{mc}(\theta, \theta')$ and $\bar{\bar{P}}^{ms}(\theta, \theta')$ for Rayleigh scatterers are

$$\bar{\bar{P}}^{mc}(\theta, \theta') = \frac{3}{8\pi} \kappa_e \tilde{\omega} \begin{bmatrix} \bar{\bar{P}}_{11}^{m} & 0 \\ 0 & \bar{\bar{P}}_{22}^{m} \end{bmatrix} \tag{109}$$

$$\bar{\bar{P}}^{ms}(\theta, \theta') = \frac{3}{8\pi} \kappa_e \tilde{\omega} \begin{bmatrix} 0 & \bar{\bar{P}}_{12}^{m} \\ \bar{\bar{P}}_{21}^{m} & 0 \end{bmatrix} \tag{110}$$

where the submatrices $\overline{\overline{P}}_{ij}^{m}$ $(i,j=1,2$ and $m=0,1,2)$ are defined by

$$\overline{\overline{P}}_{11}^{0}=\begin{bmatrix}\sin^2\theta\sin^2\theta'+\frac{1}{2}\cos^2\theta\cos^2\theta' & \frac{1}{2}\cos^2\theta\\ \frac{1}{2}\cos^2\theta' & \frac{1}{2}\end{bmatrix} \tag{111}$$

$$\overline{\overline{P}}_{22}^{0}=\begin{bmatrix}0 & 0\\ 0 & \cos\theta\cos\theta'\end{bmatrix} \tag{112}$$

$$\overline{\overline{P}}_{11}^{1}=\begin{bmatrix}2\sin\theta\sin\theta'\cos\theta\cos\theta' & 0\\ 0 & 0\end{bmatrix} \tag{113}$$

$$\overline{\overline{P}}_{22}^{1}=\begin{bmatrix}\sin\theta\sin\theta' & 0\\ 0 & \sin\theta\sin\theta'\end{bmatrix} \tag{114}$$

$$\overline{\overline{P}}_{11}^{2}=\begin{bmatrix}\frac{1}{2}\cos^2\theta\cos^2\theta' & -\frac{1}{2}\cos^2\theta\\ -\frac{1}{2}\cos^2\theta' & \frac{1}{2}\end{bmatrix} \tag{115}$$

$$\overline{\overline{P}}_{22}^{2}=\begin{bmatrix}\cos\theta\cos\theta' & 0\\ 0 & 0\end{bmatrix} \tag{116}$$

$$\overline{\overline{P}}_{12}^{1}=\begin{bmatrix}\cos\theta\sin\theta\sin\theta' & 0\\ 0 & 0\end{bmatrix} \tag{117}$$

$$\overline{\overline{P}}_{21}^{1}=\begin{bmatrix}-2\sin\theta\sin\theta'\cos\theta' & 0\\ 0 & 0\end{bmatrix} \tag{118}$$

$$\overline{\overline{P}}_{12}^{2}=\begin{bmatrix}\frac{1}{2}\cos^2\theta\cos\theta' & 0\\ -\frac{1}{2}\cos\theta' & 0\end{bmatrix} \tag{119}$$

$$\overline{\overline{P}}_{21}^{2}=\begin{bmatrix}-\cos\theta\cos^2\theta' & \cos\theta\\ 0 & 0\end{bmatrix} \tag{120}$$

Substituting (107)–(108) into the dense medium radiative transfer equation (78), carrying out the integration with respect to ϕ', and collecting terms with the same cosine or sine dependence in the azimuthal direction, we have, for $m=0,1,2$ and $0\le\phi\le\pi$,

$$\cos\theta\frac{d}{dz}\overline{I}^{mc}(\theta,z)=-\kappa_e\overline{I}^{mc}(\theta,z)+(1+\delta_m)\pi\int_0^{\pi}d\theta'\sin\theta' \times\left[\overline{\overline{P}}^{mc}(\theta,\theta')\cdot\overline{I}^{mc}(\theta',z)-\overline{\overline{P}}^{ms}(\theta,\theta')\cdot\overline{I}^{ms}(\theta',z)\right] \tag{121}$$

and

$$\cos\theta\frac{d}{dz}\bar{I}^{ms}(\theta,z) = -\kappa_e\bar{I}^{ms}(\theta,z) + (1+\delta_m)\pi\int_0^{\pi} d\theta' \sin\theta' \times\left[\bar{\bar{P}}^{ms}(\theta,\theta')\cdot\bar{I}^{mc}(\theta',z) + \bar{\bar{P}}^{mc}(\theta,\theta')\cdot\bar{I}^{ms}(\theta',z)\right] \quad (122)$$

where δ_m equals 1 as $m = 0$, and equals 0 otherwise. Equations (121) and (122) are the expressions of mth order Fourier series expansion for the dense medium radiative transfer equation (78). It is noted that $\bar{I}^{mc}(\theta,z)$ and $\bar{I}^{ms}(\theta,z)$ are coupled in (121) and (122). However, by considering the even and odd properties of $\bar{\bar{P}}^{mc}(\theta,\theta')$ and $\bar{\bar{P}}^{ms}(\theta,\theta)$, we can define two quantities $\bar{I}^{me}(\theta,z)$ and $\bar{I}^{mo}(\theta,z)$ as [10,11]

$$\bar{I}^{me}(\theta,z) = \begin{bmatrix} I_v^{mc}(\theta,z) \\ I_h^{mc}(\theta,z) \\ U^{ms}(\theta,z) \\ V^{ms}(\theta,z) \end{bmatrix}; \qquad \bar{I}^{mo}(\theta,z) = \begin{bmatrix} I_v^{ms}(\theta,z) \\ I_h^{ms}(\theta,z) \\ U^{mc}(\theta,z) \\ V^{mc}(\theta,z) \end{bmatrix} \quad (123)$$

such that $\bar{I}^{mo}(\theta,z)$ and $\bar{I}^{me}(\theta,z)$ can be solved independently. The symbols e and o are used to denote the even and odd terms, because the first two elements in $\bar{I}^{me}(\theta,z)$ and $\bar{I}^{mo}(\theta,z)$ are related to cosine and sine functions of azimuthal angles respectively.

We further let $\bar{I}^{m\alpha}(\theta,z)$ and $\bar{I}^{m\alpha}(\pi-\theta,z)$, $\alpha = e,o$, and $0 \le \theta \le \pi/2$, represent the intensities propagating upward and downward respectively. Equations (121) and (122) can be decomposed into

$$\cos\theta\frac{d}{dz}\bar{I}^{m\alpha}(\theta,z) = -\kappa_e\bar{I}^{m\alpha}(\theta,z) + (1+\delta_m)\pi\int_0^{\pi/2} d\theta' \sin\theta' \times\left[\bar{\bar{P}}^{m\alpha}(\theta,\theta')\cdot\bar{I}^{m\alpha}(\theta',z) + \bar{\bar{P}}^{m\alpha}(\theta,\pi-\theta')\cdot\bar{I}^{m\alpha}(\pi-\theta',z)\right] \quad (124)$$

and

$$\cos\theta\frac{d}{dz}\bar{I}^{m\alpha}(\pi-\theta,z) = -\kappa_e\bar{I}^{m\alpha}(\pi-\theta,z) + (1+\delta_m)\pi\int_0^{\pi/2} d\theta' \sin\theta' \times\left[\bar{\bar{P}}^{m\alpha}(\pi-\theta,\theta')\cdot\bar{I}^{m\alpha}(\theta',z) + \bar{\bar{P}}^{m\alpha}(\pi-\theta,\pi-\theta')\cdot\bar{I}^{m\alpha}(\pi-\theta',z)\right] \quad (125)$$

for $m = 0, 1, 2$. The matrices $\overline{\overline{P}}^{m\alpha}(\theta, \theta')$ can be defined in terms of $\overline{\overline{P}}_{ij}^{m}$ of (111)–(120) as

$$\overline{\overline{P}}^{me}(\theta, \theta') = \frac{3}{8\pi}\kappa_e\tilde{\omega}\begin{bmatrix} \overline{\overline{P}}_{11}^{m} & -\overline{\overline{P}}_{12}^{m} \\ \overline{\overline{P}}_{21}^{m} & \overline{\overline{P}}_{22}^{m} \end{bmatrix} \tag{126}$$

$$\overline{\overline{P}}^{mo}(\theta, \theta') = \frac{3}{8\pi}\kappa_e\tilde{\omega}\begin{bmatrix} \overline{\overline{P}}_{11}^{m} & \overline{\overline{P}}_{12}^{m} \\ -\overline{\overline{P}}_{21}^{m} & \overline{\overline{P}}_{22}^{m} \end{bmatrix} \tag{127}$$

The corresponding boundary conditions without ϕ-dependence can be derived by expanding the incident Stokes vector $\overline{I}_o(\pi - \theta_o, \phi_o)$ into Fourier series [10,11],

$$\overline{I}_o(\pi - \theta, \phi) = \overline{I}_o\delta(\cos\theta - \cos\theta_o)\sum_{m=0}^{\infty}\left[\frac{1}{(1+\delta_m)\pi}\cos m(\phi - \phi_o)\right] \tag{128}$$

Substituting the above expression (128) into equations (90) and (91), the boundary conditions become, for $0 \le \theta \le \pi/2$ and $m = 0, 1, 2$, at $z = 0$

$$\overline{I}^{m\alpha}(\pi - \theta, z = 0) = \overline{\overline{T}}_{01}(\theta_o)\cdot\overline{I}_o^{m\alpha}(\pi - \theta_o) + \overline{\overline{R}}_{10}(\theta)\cdot\overline{I}^{m\alpha}(\theta, z = 0) \tag{129}$$

and at $z = -d$

$$\overline{I}^{m\alpha}(\theta, z = -d) = \overline{\overline{R}}_{12}(\theta)\cdot\overline{I}^{m\alpha}(\pi - \theta, z = -d) \tag{130}$$

where

$$\overline{I}_o^{m\alpha}(\pi - \theta) = \frac{1}{(1+\delta_m)\pi}\overline{I}_o^{m\alpha}\delta(\cos\theta - \cos\theta_o) \tag{131}$$

with

$$\overline{I}_o^{me} = \begin{bmatrix} I_{vo} \\ I_{ho} \\ 0 \\ 0 \end{bmatrix}; \qquad \overline{I}_o^{mo} = \begin{bmatrix} 0 \\ 0 \\ U_o \\ V_o \end{bmatrix} \tag{132}$$

To solve the radiative transfer equations numerically, the total intensity is decomposed into reduced intensity and diffuse intensity [34]. In doing so, we were able to overcome some numerical difficulties encountered in matching boundary conditions for discretized intensities.

We also find some differences in numerical results between the total intensity approach and the decomposition approach. We can write

$$\overline{I}^{m\alpha} = \overline{I}_{ri}^{m\alpha} + \overline{I}_{d}^{m\alpha} \tag{133}$$

where $\overline{I}_{ri}^{m\alpha}$ and $\overline{I}_{d}^{m\alpha}$ represent the reduced and diffuse intensities respectively. The reduced intensity for the incident Stokes vector $\overline{I}_o(\pi-\theta_o, \phi_o)$ of (128) can be obtained as

$$\overline{I}_{ri}^{m\alpha}(\theta, z) = \frac{1}{(1+\delta_m)\pi} e^{-\kappa_e z/\cos\theta} \overline{\overline{F}}(\theta) \cdot \overline{\overline{R}}_{12}(\theta) e^{-2\kappa_e d/\cos\theta} \cdot \overline{\overline{T}}_{01}(\theta_o) \cdot \overline{I}_o^{m\alpha} \delta(\cos\theta - \cos\theta_o) \tag{134}$$

and

$$\overline{I}_{ri}^{m\alpha}(\pi-\theta, z) = \frac{1}{(1+\delta_m)\pi} e^{\kappa_e z/\cos\theta} \overline{\overline{F}}(\theta) \cdot \overline{\overline{T}}_{01}(\theta_o) \cdot \overline{I}_o^{m\alpha} \delta(\cos\theta - \cos\theta_o) \tag{135}$$

where $\overline{\overline{F}}(\theta)$, a matrix which characterizes the effect of dielectric slab on the incident intensity, is defined as

$$\overline{\overline{F}}(\theta) = \left[\overline{\overline{I}} - \overline{\overline{R}}_{10}(\theta) \cdot \overline{\overline{R}}_{12}(\theta) e^{-2\kappa_e d/\cos\theta}\right]^{-1} \tag{136}$$

with $\overline{\overline{I}}$ being the identity matrix.

Then, the diffuse intensities satisfy the following equations for $0 \leq \theta \leq \pi/2$

$$\begin{aligned}
&\cos\theta \frac{d}{dz} \overline{I}_d^{m\alpha}(\theta, z) = \\
&-\kappa_e \overline{I}_d^{m\alpha}(\theta, z) + (1+\delta_m)\pi \int_0^{\pi/2} d\theta' \sin\theta' \\
&\times \left\{\overline{\overline{P}}^{m\alpha}(\theta, \theta') \cdot \overline{I}_d^{m\alpha}(\theta', z) + \overline{\overline{P}}^{m\alpha}(\theta, \pi-\theta') \cdot \overline{I}_d^{m\alpha}(\pi-\theta', z)\right\} \\
&+ \overline{S}_1^{m\alpha}(\theta, \theta_p) e^{-\kappa_e z/\cos\theta_p} + \overline{S}_2^{m\alpha}(\theta, \theta_p) e^{\kappa_e z/\cos\theta_p}
\end{aligned} \tag{137}$$

and

$$\begin{aligned}
&-\cos\theta \frac{d}{dz} \overline{I}_d^{m\alpha}(\pi-\theta, z) = \\
&-\kappa_e \overline{I}_d^{m\alpha}(\pi-\theta, z) + (1+\delta_m)\pi \int_0^{\pi/2} d\theta' \sin\theta' \\
&\times \left\{\overline{\overline{P}}^{m\alpha}(\pi-\theta, \theta') \cdot \overline{I}_d^{m\alpha}(\theta', z) + \overline{\overline{P}}^{m\alpha}(\pi-\theta, \pi-\theta') \cdot \overline{I}_d^{m\alpha}(\pi-\theta', z)\right\} \\
&+ \overline{S}_1^{m\alpha}(\pi-\theta, \theta_p) e^{-\kappa_e z/\cos\theta_p} + \overline{S}_2^{m\alpha}(\pi-\theta, \theta_p) e^{\kappa_e z/\cos\theta_p}
\end{aligned} \tag{138}$$

where θ_p is the transmitted angle in region 1 for the incident angle θ_o from region 0 upon the slab. The matrices $\overline{S}_1^{m\alpha}$ and $\overline{S}_2^{m\alpha}$ in (137) and (138) account for the scattering of reduced intensity into the diffuse intensity. They represent source terms propagating upward and downward respectively. They are

$$\overline{S}_1^{m\alpha}(\theta,\theta_p) = \frac{\epsilon_o \cos\theta_o}{\epsilon_1 \cos\theta_p}\overline{\overline{P}}^{m\alpha}(\theta,\theta_p)\cdot\overline{\overline{F}}(\theta_p) \cdot \overline{\overline{R}}_{12}(\theta_p)e^{-2\kappa_e d/\cos\theta_p}\cdot\overline{\overline{T}}_{01}(\theta_o)\cdot\overline{I}_o^{m\alpha} \quad (139)$$

$$\overline{S}_2^{m\alpha}(\theta,\theta_p) = \frac{\epsilon_o \cos\theta_o}{\epsilon_1 \cos\theta_p}\overline{\overline{P}}^{m\alpha}(\theta,\pi-\theta_p)\cdot\overline{\overline{F}}(\theta_p)\cdot\overline{\overline{T}}_{01}(\theta_o)\cdot\overline{I}_o^{m\alpha} \quad (140)$$

where ϵ_1 is the real part of the effective permittivity in region 1. It is seen from (139) and (140) that $\overline{S}_1^{m\alpha}$ and $\overline{S}_2^{m\alpha}$ are closely related to the polarization state of incident waves. The corresponding boundary conditions for the diffuse intensities are

$$\overline{I}_d^{m\alpha}(\pi-\theta, z=0) = \overline{\overline{R}}_{10}(\theta)\cdot\overline{I}_d^{m\alpha}(\theta, z=0) \quad (141)$$

for $0 \le \theta \le \pi/2$ at $z = 0$, and

$$\overline{I}_d^{m\alpha}(\theta, z=-d) = \overline{\overline{R}}_{12}(\theta)\cdot\overline{I}_d^{m\alpha}(\pi-\theta, z=-d) \quad (142)$$

for $0 \le \theta \le \pi/2$ at $z = -d$. In past remote sensing applications where either vertical or horizontal incident polarized waves are used, it is sufficient to just solve the radiative transfer equation with even α. However, for polarimetric applications, all possible polarizations of incident waves will be considered and the Mueller matrix with 4×4 elements are also calculated. Both radiative transfer equations of $\alpha = e, o$ are to be solved numerically for four independent polarized states of incident Stokes vectors, viz. vertical, horizontal, linear with 45° orientation, and left-hand circular polarizations.

The set of equations (137) and (138) without ϕ–dependence are solved using the method of Gauss' quadrature [11,34]. The integrals in the transfer equations are replaced by appropriately weighted sums over $2N$ intervals between the $2N$ zeros of the even-order Legendre polynomial $P_{2N}(\theta)$. Thus, for each harmonic index m ($m \le 2$ for Rayleigh scatterers), the system of first-order differential equations can be solved by using the discrete ordinate eigen-analysis approach and

by matching the boundary conditions (141) and (142). The solutions are evaluated only at the Gauss' quadrature angles θ_j, $j = 1, 2, \cdots, N$. A self consistent intensity interpolation scheme [11,34] is then used to calculate the scattered intensities and Mueller matrices at all other angles. Once the solutions are obtained, we can reconstruct their ϕ–dependence and calculate the scattered intensities in direction (θ, ϕ) by using equation (107).

d. Comparison with Laboratory Experiments

A major objective of the dense medium radiative transfer theory (DMT) is to provide an adequate theoretical approach for studying the characteristics of dense discrete random media and the effects on electromagnetic waves propagating and scattering in such media. The purpose of this section is to validate our theoretical models by comparison with data from controlled laboratory experiments [24–26]. There are at least two advantages in controlled laboratory experiments. First, all the parameters of the target scatterers are known. Second, one can study the electromagnetic response by varying one particular physical parameter of interest while keeping others constant, which is generally difficult in field experiments. For this purpose, the results of coherent wave attenuation rates and bistatic scattered intensities as functions of particle concentration from controlled laboratory experiments are compared with theoretical computations.

The experiments were conducted by Ishimaru and Kuga [24–26]. The laboratory discrete random medium comprises of a collection of Latex spheres suspended in a spectrophotometer cell with water. The indices of refraction for Latex spheres, water and glass container are 1.588, 1.33 and 1.47 respectively. The experiments were performed by using a He-Ne laser light ($\lambda = 0.6328\mu m$) and attenuation rates and bistatic intensities were measured over a wide range of concentrations from 0.001% to 30%. The measurement data of attenuation rates and bistatic intensities were normalized in a proper way. The attenuation rate was normalized by the value of attenuation rate of independent scattering at fractional volume of 100%. The bistatic scattered intensities were normalized by the total transmitted intensity of laser light through the water and the glass container in the absence of Latex spheres.

The numerical solutions from the dense medium radiative transfer theory are used to interpret the controlled laboratory experimen-

tal data. The intensity interpolation scheme [34] was used to compute bistatic scattered intensities at arbitrary scattered angle, since the laser light is normally incident upon the sample cell containing scatterers embedded in water and the detector scans the bistatic scattered flux over a small range of angles around the backscattering direction in the experiments. The present theoretical computations are limited to single size particles, an equivalent diameter of $0.078\mu m$ is used. A loss tangent of 10^{-6} is introduced to account for a slight absorption loss in the Latex spheres. Bistatic intensities are illustrated in linear scale, the backward flux density received by the detector with a particular field of view (FOV) is calculated by using the formula $F = \pi\theta_o^2 I$, where I is the bistatic intensity, and θ_o is the half angle of FOV. In this numerical calculation, $\theta_o = 0.1°$ and the thickness of the scattering layer is $10mm$. For comparison, we also show the numerical calculations based on the conventional radiative transfer theory (CRT) which assumes the independent scattering between scatterers.

The measured and calculated attenuation rates and bistatic scattered intensities are shown in Figs. 2.10 and 2.11 respectively, where the circles represent the measured results and solid lines denote the theoretical results of CRT and DMT. Fig. 2.10 illustrates the attenuation rate as a function of fractional volume of particles. Equation (60) with $L = 1$ is used for the calculation of DMT attenuation rates. All the calculated results of DMT and CRT are normalized in the same way as those in the experiment. It is seen that the measured attenuation rate reaches a maximum at about $f = 10\%$, and then decrease as the fractional volume further increases. This indicates that the medium appears more homogeneous when the fractional volume of inhomogeneities increase beyond a certain value. The results of DMT are in good agreement with these experimental features while CRT predicts a monotonic increase with concentration and higher attenuation rates than both DMT and the experiment.

Fig. 2.11 illustrates the bistatic scattered intensity as a function of fractional volume. In Fig. 2.2 of reference [26], the backscattering intensities are plotted as a function of observation angles for different concentrations (from 0.302% to 28.95%). We plotted here the bistatic intensities as a function of concentration at a fixed observation angle (4°). A similar behavior is observed for the bistatic intensity. With increasing fractional volume greater than 10%, the measured bistatic intensities at observation angle of 4° begin to decrease as shown in

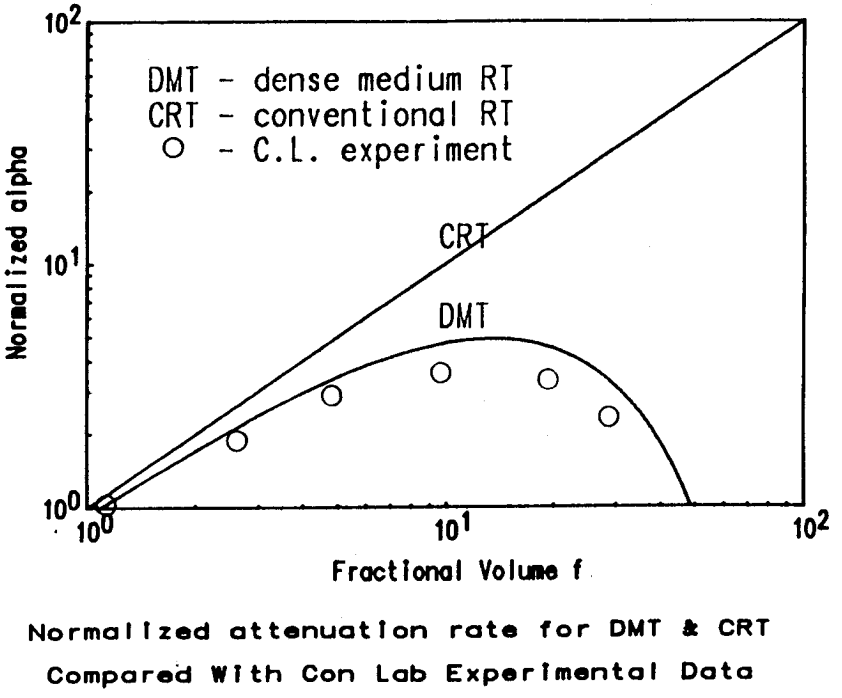

Figure 2.10 Normalized attenuation rate as a function of fractional volume of Latex spheres. The dense medium radiative transfer theory (DMT) and conventional radiative transfer theory (CRT) results are compared with the experimental data (○). The wavelength of laser light is 0.6328μm, the index of refraction is 1.588 for Latex spheres and 1.332 for water, and the equivalent diameter of Latex spheres is 0.078μm.

Fig. 2.11. The results of dense medium radiative transfer equation contain these experimental features. On the other hand, the results of conventional radiative transfer theory predict a monotonic increase with concentration. The reason for choosing a 4° bistatic angle instead of 0° is that there is a backscattering enhancement in the exact backscattering direction with a small angular width of about 0.2° which is due

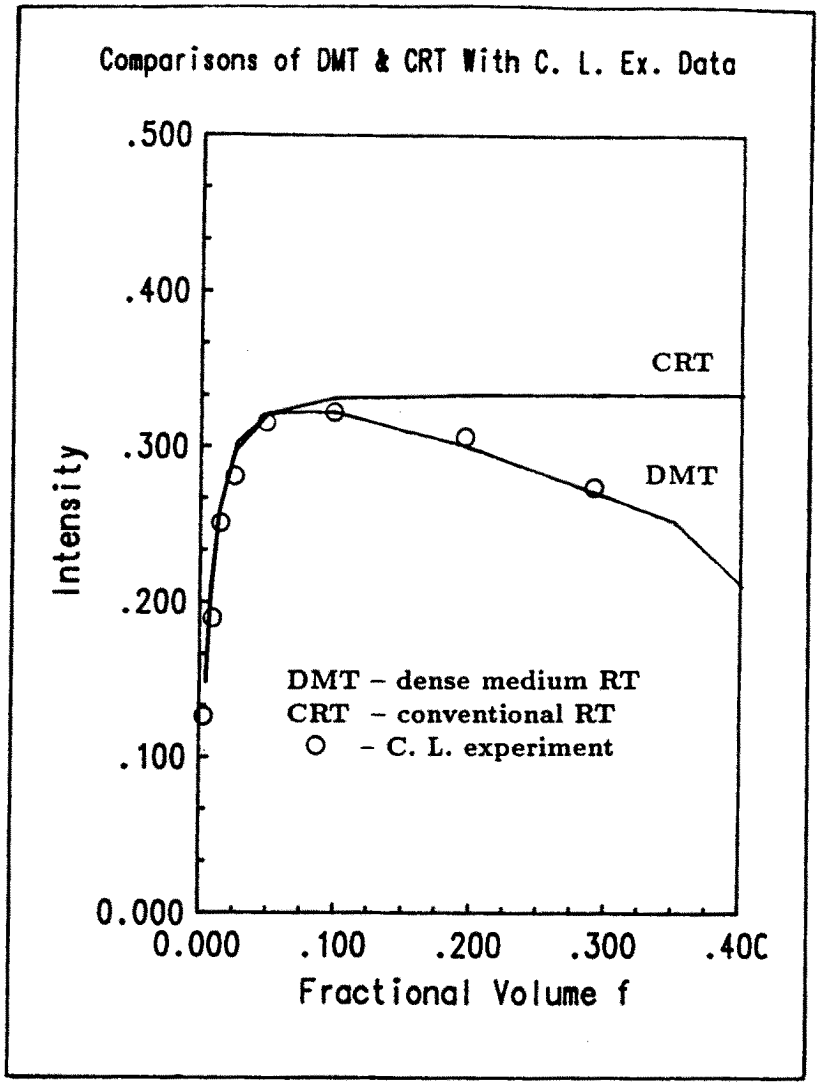

Figure 2.11 Normalized bistatic intensities as a function of fractional volume of Latex spheres. The dense medium radiative transfer theory (DMT) and conventional radiative transfer theory (CRT) results are compared with the experimental data (o). The wavelength of laser light is $0.6328\mu m$, the index of refraction is 1.588 plus a 10^{-6} loss tangent for Latex spheres and 1.332 for water, the equivalent diameter of Latex spheres is $0.078\mu m$, and the slab width is $10mm$.

f(%)	EXP		DMT		CRT	
	linear	dB	linear	dB	linear	dB
0.302	0.1256	−59.2	0.1488	−58.46	0.1502	−58.42
0.603	0.1858	−57.5	0.2060	−57.05	0.2082	−57.01
1.206	0.2507	−56.2	0.2584	−56.07	0.2595	−56.05
2.413	0.2813	−55.7	0.3027	−55.38	0.2980	−55.45
4.825	0.3156	−55.2	0.3219	−55.11	0.3215	−55.12
9.650	0.3229	−55.1	0.3227	−55.10	0.3317	−54.98
19.30	0.3084	−55.3	0.3014	−55.40	0.3340	−54.95
28.95	0.2748	−55.8	0.2715	−55.85	0.3341	−54.95

Table 2.1

to the including of cyclical scattering terms [11]. In Tab. 1, the experimental data and the numerical results of bistatic intensity of DMT and CRT are also listed in both linear and logarithmic scales. As shown in the table, a good agreement can be found between the results of the dense medium radiative transfer theory and the experiment.

From these results, both the attenuation rate and bistatic scattered intensity show nonlinear behaviors that strongly relate to the changes in particles concentration. These features cannot be explained by the conventional radiative transfer theory.

e. Numerical Results of Radar Polarimetry

In this section we illustrate the numerical results of radar polarimetry for a slab of snow medium with ice particles having size distributions. The ice particles in snow usually have sizes ranging from $0.01mm$ to $2mm$. The parameters chosen here represent some typical values in the microwave remote sensing of snow media. The ice particle size is assumed to follow a modified gamma distribution described by equation (73). The input parameters for this model are indices P, Q, mode size a_c, and total fractional volume of particles f_{tot}. The size distribution is discretized into thirty different sizes and the pair distribution functions are also calculated.

In Figs. 2.12(a), (b) and (c), we plot the copolarization signature, depolarization signature and degree of polarization respectively as a function of ellipticity angle χ and orientation angle ψ of the incident

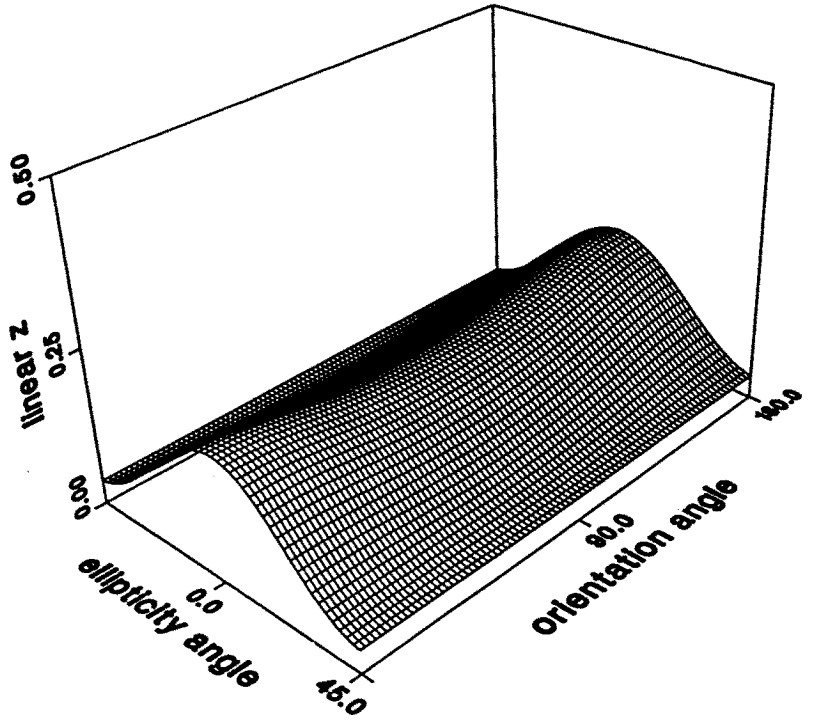

Figure 2.12a Polarization signatures of a layer of densely distributed spherical particles based on the dense medium radiative transfer theory as a function of ellipticity angle χ and polarization orientation angle ψ. Other parameters are as follows. $frequency = 17GHz$, $\epsilon_s = (3.2+i0.002)\epsilon_o$, $d = 27cm$, $\epsilon_2 = (6+i0.6)\epsilon_o$, $\theta_o = 40.8°$. **The particle size distribution is described by** $P = 6$, $Q = 4$, $a_c = 0.1cm$, **and** $f_{tot} = 0.2$. **(12a) copolarization coefficient** ($\sigma = 0.196$ **at** $\psi = 180°$, $\chi = 0°$).

waves at $\theta_o = 40.8°$. The particle size distribution has a mode radius at $a_c = 0.1cm$ and $f_{tot} = 0.2$. We note that the horizontal polarization produce larger return than the vertical polarization, while circular polarizations give minimum return which is independent of orientation angle. The copolarization also shows a pedestal that has been observed in SAR polarimetric radar data [9]. In Fig. 2.12(b), the depolarization coefficient shows a maximum for circular polarizations. In Fig. 2.12(c), the degree of polarization is plotted. The values of degree of polarization demonstrate that the multiple scattering mechanism produces the unpolarized wave return.

In Figs. 2.13(a), (b) and (c), the mode radius of size distribution

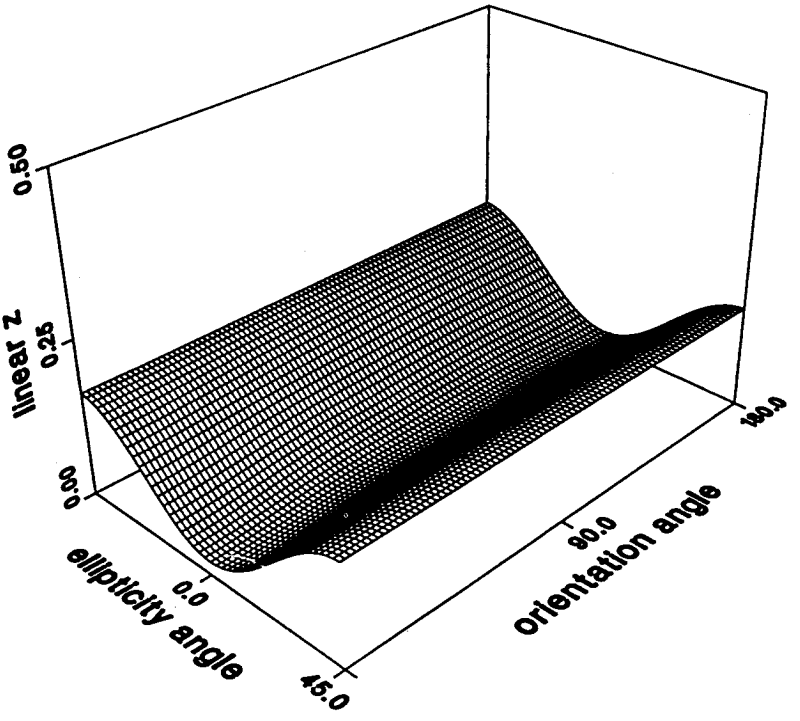

Figure 2.12b Depolarization coefficient ($\sigma_d = 0.165$ **at** $\psi = 180°$, $\chi = -45°$).

is changed to a higher value $a_c = 0.125cm$. The copolarization signature in Fig. 2.13(a) shows a larger pedestal than in Fig. 2.12(a), while the degree of polarization is decreased dramatically in Fig. 2.13(c). This is because the larger particles can contribute significantly to the scattering effects and increase more the unpolarized power return. In Figs 2.14 and 2.15, the polarization signatures and the degree of polarization are plotted for different incidence angles $\theta_o = 69.1°$ and $17.2°$ respectively. It shows that for larger incidence angle the polarization coefficients and degree of polarization exhibit larger variations.

2.4 Conclusions

In this chapter, we have demonstrated the usefulness of the vector radiative transfer theory for studying polarimetric signatures of random discrete scatterers. In the case of sparse concentration of nonspherical particles, we have used the non-diagonal extinction matrix

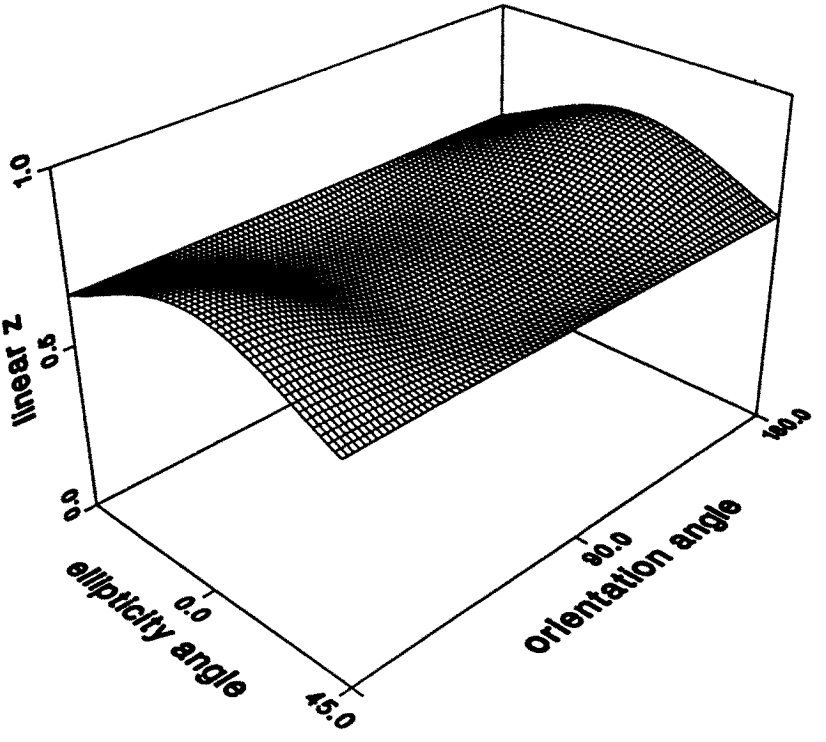

Figure 2.12c Degree of polarization.

to account for the attenuation rate, propagation constant and phase difference between the two characteristic polarizations. This permits the explanation of the phase difference between *vv* and *hh* signatures that have been observed experimentally in data of polarimetric remote sensing. We have studied the effects of orientation distributions. We have shown that the increase of variance of orientation corresponds to the increase of heterogeneity of scatterers and directly contributes to partial polarization of the return signal. We have also studied the effects of second order scattering.

For the case of dense medium with appreciable fractional volume of particles, we have included the effects of correlated scatterers and have corrected the deficiencies of independent scattering that is inherent in the conventional radiative theory. The dense medium radiative transfer theory explains the features of dependence on concentration observed in laboratory controlled experiments. We have studied the effects of multiple scattering and effects of correlated scatterers governed by particle size distribution. We have shown that generally multiple

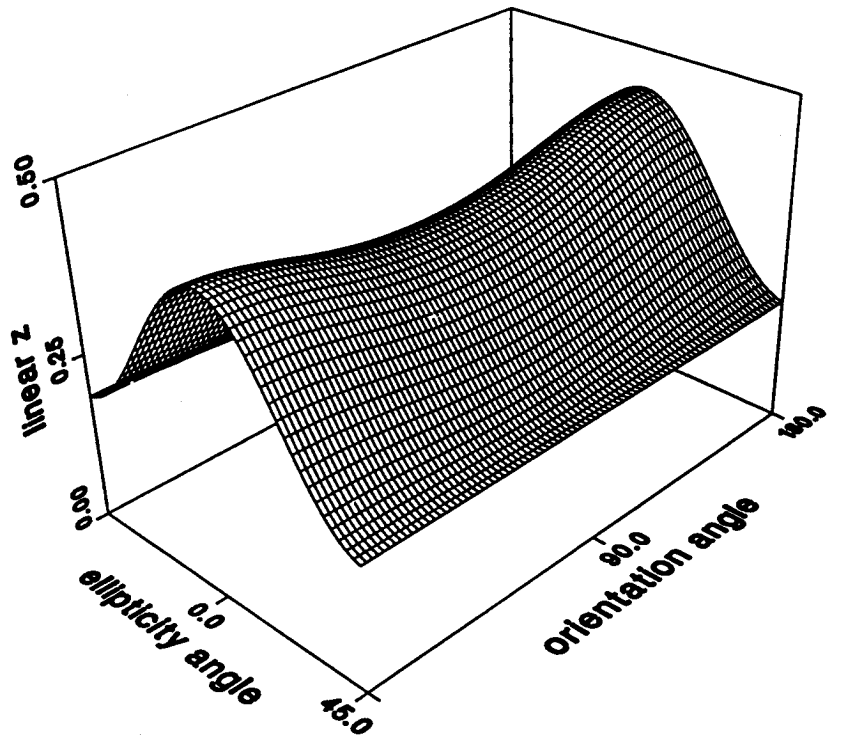

Figure 2.13a Polarization signatures of a layer of densely distributed spherical particles based on the dense medium radiative transfer theory as a function of ellipticity angle χ and polarization orientation angle ψ. Other parameters are as follows. *frequency* $= 17GHz$, $\epsilon_s = (3.2+i0.002)\epsilon_o$, $d = 27cm$, $\epsilon_2 = (6 + i0.6)\epsilon_o$, $\theta_o = 40.8°$. **The particle size distribution is described by** $P = 6$, $Q = 4$, $a_c = 0.125cm$, **and** $f_{tot} = 0.2$. **(13a) copolarization coefficient** ($\sigma = 0.440$ **at** $\psi = 180°$, $\chi = 0°$).

scattering can cause a pedestal in return signal and can also decrease polarization contrast.

Appendix

In this Appendix, we list the extinction matrix elements and phase matrix elements for small spheroids that are uniformly oriented in the Eulerian angle γ.

Consider a spheroid with semi-axes lengths $a, b = a$, and c respectively in $\hat{x}_b$, $\hat{y}_b$, and $\hat{z}_b$ directions. The $(\hat{x}_b, \hat{y}_b, \hat{z}_b)$ natural axes directions are related to principal coordinates direction $(\hat{x}, \hat{y}, \hat{z})$ by the Euler angles α, β, and γ [11,p.158–160]. The scattering amplitudes

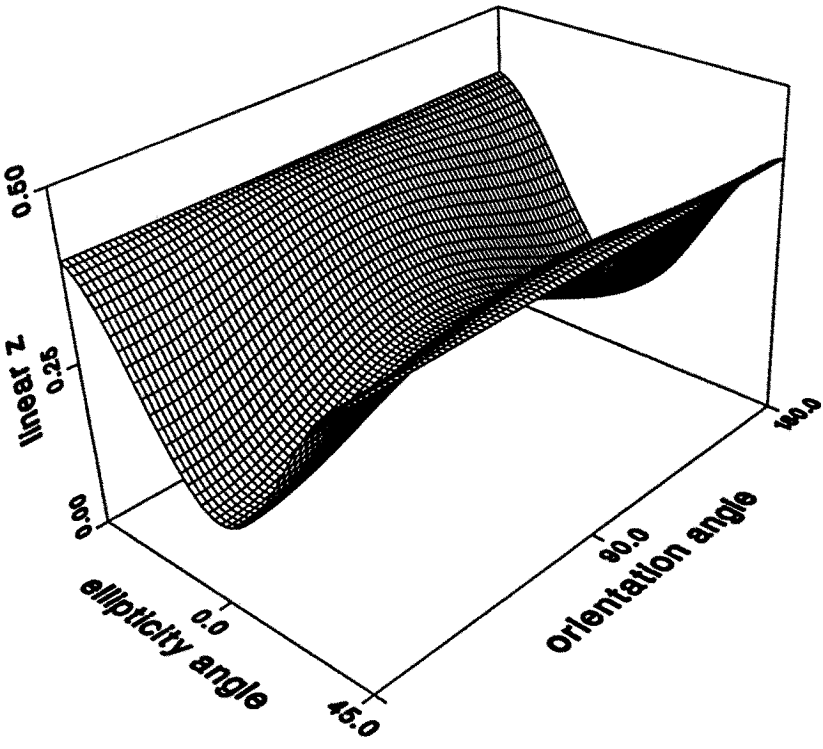

Figure 2.13b Depolarization coefficient ($\sigma_d = 0.397$ at $\psi = 180°$, $\chi = -45°$).

$f_{jl}(\theta, \phi; \theta', \phi'; \beta, \gamma)$ will be independent of α. In line with the reasoning in section 2.3 concerning the extinction matrix, we calculate the scattering amplitudes and include the leading term in the real part and the leading term in the imaginary part. Thus

$$f_{vv}(\theta, \phi; \theta', \phi'; \beta, \gamma) = \frac{3}{2ik}\left\{T_1(\hat{\theta}\cdot\hat{\theta}') + (T_0 - T_1)(\hat{\theta}\cdot\hat{z}_b)(\hat{z}_b\cdot\hat{\theta}')\right\} \tag{A.1}$$

$$f_{vh}(\theta, \phi; \theta', \phi'; \beta, \gamma) = \frac{3}{2ik}\left\{T_1(\hat{\theta}\cdot\hat{\phi}') + (T_0 - T_1)(\hat{\theta}\cdot\hat{z}_b)(\hat{z}_b\cdot\hat{\phi}')\right\} \tag{A.2}$$

$$f_{hv}(\theta, \phi; \theta', \phi'; \beta, \gamma) = \frac{3}{2ik}\left\{T_1(\hat{\phi}\cdot\hat{\theta}') + (T_0 - T_1)(\hat{\phi}\cdot\hat{z}_b)(\hat{z}_b\cdot\hat{\theta}')\right\} \tag{A.3}$$

$$f_{hh}(\theta, \phi; \theta', \phi'; \beta, \gamma) = \frac{3}{2ik}\left\{T_1(\hat{\phi}\cdot\hat{\phi}') + (T_0 - T_1)(\hat{\phi}\cdot\hat{z}_b)(\hat{z}_b\cdot\hat{\phi}')\right\} \tag{A.4}$$

where [11, p. 193]

$$T_0 = it_0 - t_0^2 \tag{A.5}$$

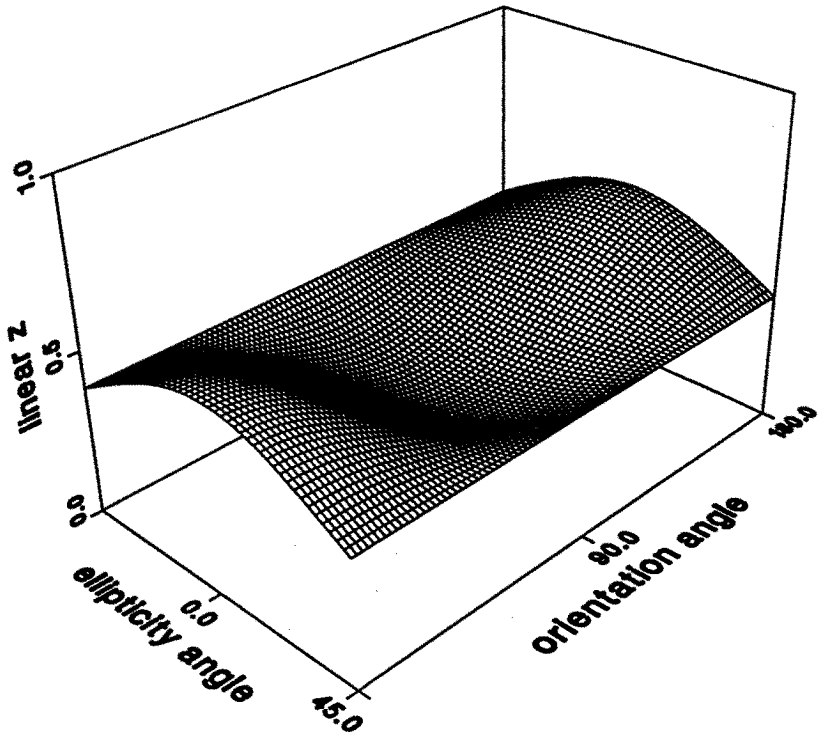

Figure 2.13c Degree of polarization.

$$T_1 = it_1 - t_1^2 \tag{A.6}$$

$$t_0 = \frac{2}{9}\frac{k^3a^2c\,(\epsilon_s/\epsilon - 1)}{(1 + v_d A_c)} \tag{A.7}$$

$$t_1 = \frac{2}{9}\frac{k^3a^2c\,(\epsilon_s/\epsilon - 1)}{(1 + v_d A_a)} \tag{A.8}$$

The usual scattering amplitudes of small spheroids (A.1)–(A.8) only contain the first term in (A.5) and (A.6) for T_0 and T_1. However, in applying the extinction matrix formulas, we need the leading term of the real part and the leading term of the imaginary part. Thus, the second terms in (A.5) and (A.6) are necessary.

In (A.7)–(A.8)

$$A_a = \frac{1}{a^2c} - \frac{A_c}{2} \tag{A.9}$$

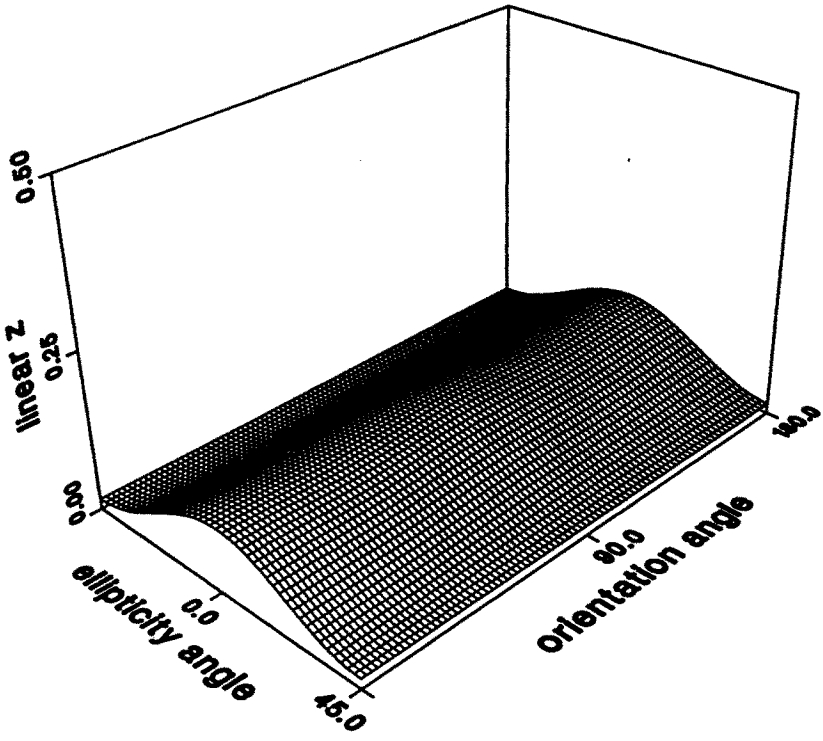

Figure 2.14a Polarization signatures of a layer of densely distributed spherical particles based on the dense medium radiative transfer theory as a function of ellipticity angle χ and polarization orientation angle ψ. Other parameters are as follows. *frequency* $= 17GHz$, $\epsilon_s = (3.2+i0.002)\epsilon_o$, $d = 27cm$, $\epsilon_2 = (6 + i0.6)\epsilon_o$, $\theta_o = 69.1°$. **The particle size distribution is described by** $P = 6$, $Q = 4$, $a_c = 0.125cm$, **and** $f_{tot} = 0.2$. **(14a) copolarization coefficient** ($\sigma = 9.951 \times 10^{-2}$ **at** $\psi = 180°$, $\chi = 0°$).

where for oblate spheroids $(a > c)$

$$A_c = \frac{2}{(a^2 - c^2)^{3/2}} \left[\frac{\sqrt{a^2 - c^2}}{c} - \tan^{-1} \frac{\sqrt{a^2 - c^2}}{c} \right] \tag{A.10}$$

and for prolate spheroids $(c > a)$

$$A_c = \frac{2}{(c^2 - a^2)^{3/2}} \left[\frac{2\sqrt{c^2 - a^2}}{c} + \ln \frac{c - \sqrt{c^2 - a^2}}{c + \sqrt{c^2 - a^2}} \right] \tag{A.11}$$

In (A.1)–(A.8), $v_d = a^2 c(\epsilon_s/\epsilon - 1)/2$ and

$$\hat{z}_b = -\cos\gamma \sin\beta \hat{x} + \sin\gamma \sin\beta \hat{y} + \cos\beta \hat{z} \tag{A.12}$$

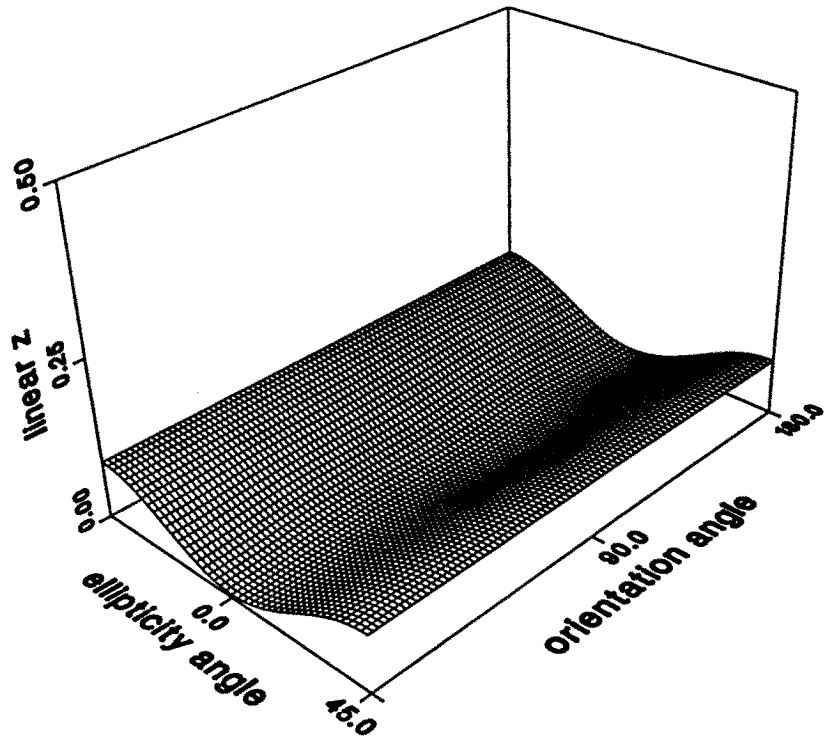

Figure 2.14b Depolarization coefficient ($\sigma_d = 8.801 \times 10^{-2}$ **at** $\psi = 180°$, $\chi = -45°$).

is the direction of the symmetry axis of the spheroid, $(\hat{\theta}, \hat{\phi})$ are the spherical unit vectors in direction (θ, ϕ) and $(\hat{\theta}', \hat{\phi}')$ are the spherical unit vectors in direction (θ', ϕ').

The Eulerian angles are as defined in reference 11, p.158. The angle γ is the azimuthal angle of the symmetry axis while the angle β is the angle that the symmetry axis $\hat{z}_b$ of the spheroid makes with the $\hat{z}$ axis. We assume that the spheroids are uniformly distributed in γ between 0 and 2π. Hence, an averaging over function g is performed by

$$\langle g \rangle = \frac{1}{2\pi} \int_0^{2\pi} d\gamma \int_0^{\pi} d\beta \, p(\beta) \, g \tag{A.13}$$

The averaged forward scattering amplitudes assume the following form.

$$\langle f_{vv}(\theta, \phi; \theta, \phi) \rangle = \frac{3}{2ik} \left\{ T_1 + (T_0 - T_1) \left[\sin^2 \theta \langle \cos^2 \beta \rangle + \frac{\cos^2 \theta}{2} \langle \sin^2 \beta \rangle \right] \right\} \tag{A.14}$$

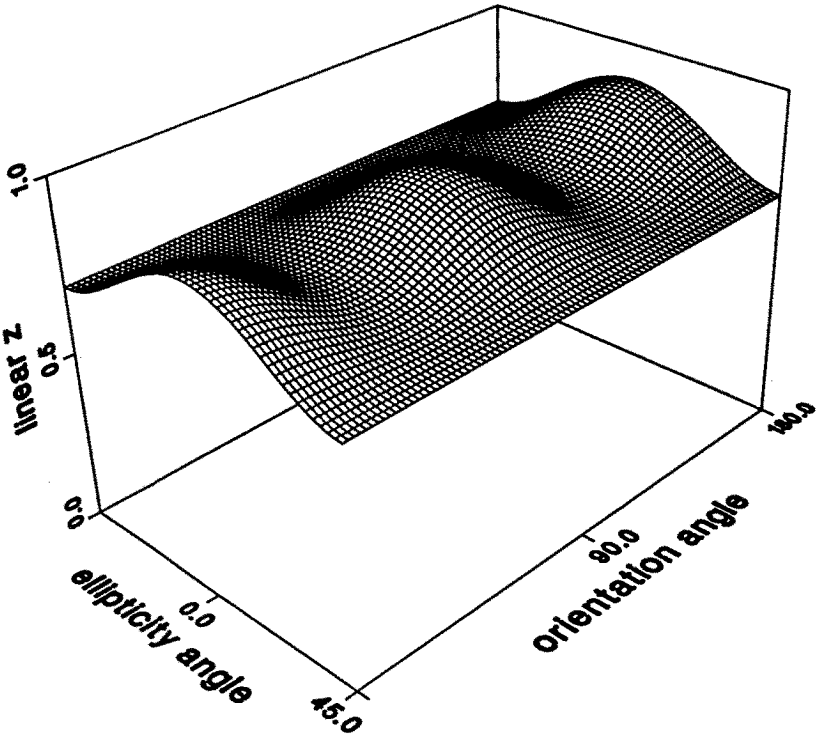

Figure 2.14c Degree of polarization.

$$\langle f_{hh}(\theta,\phi;\theta,\phi)\rangle = \frac{3}{2ik}\left\{T_1 + \frac{(T_0 - T_1)}{2}\langle \sin^2\beta\rangle\right\} \tag{A.15}$$

and

$$\langle f_{vh}(\theta,\phi;\theta,\phi)\rangle = \langle f_{hv}(\theta,\phi;\theta,\phi)\rangle = 0 \tag{A.16}$$

According to section 2.2b, the characteristic polarizations for this case are vertical and horizontal polarized waves. The expressions in (34), (35) and (36) can be used respectively for propagation constants K_1 and K_2 and eigenmatrix $\overline{\overline{E}}$ respectively.

By taking products of the scattering amplitudes in (A.1)–(A.4) and taking averaging, the phase matrix elements can be expressed as follows:

$$\overline{\overline{P}}(\theta,\phi;\theta',\phi') = \overline{\overline{P}}^{o}(\theta,\theta') + \sum_{m=1}^{2}\left[\overline{\overline{P}}^{mc}\cos m(\phi-\phi') + \overline{\overline{P}}^{ms}(\theta,\theta')\sin m(\phi-\phi')\right] \tag{A.17}$$

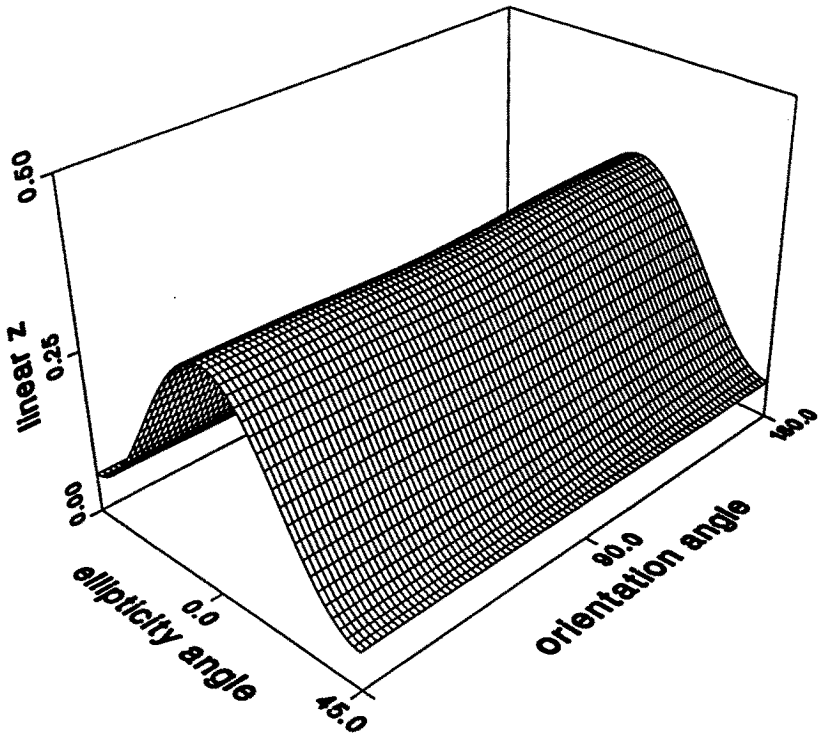

Figure 2.15a Polarization signatures of a layer of densely distributed spherical particles based on the dense medium radiative transfer theory as a function of ellipticity angle χ and polarization orientation angle ψ. Other parameters are as follows. *frequency* $= 17GHz$, $\epsilon_s = (3.2+i0.002)\epsilon_o$, $d = 27cm$, $\epsilon_2 = (6 + i0.6)\epsilon_o$, $\theta_o = 17.2°$. The particle size distribution is described by $P = 6$, $Q = 4$, $a_c = 0.125cm$, and $f_{tot} = 0.2$. (15a) copolarization coefficient ($\sigma = 0.338$ at $\psi = 180°$, $\chi = 0°$).

where

$$\overline{\overline{P}}^{o}(\theta,\theta') = \begin{bmatrix} P_{11}^{o} & P_{12}^{o} & 0 & 0 \\ P_{21}^{o} & P_{22}^{o} & 0 & 0 \\ 0 & 0 & 0 & 0 \\ 0 & 0 & 0 & P_{44}^{o} \end{bmatrix} \tag{A.18}$$

$$\overline{\overline{P}}^{1c}(\theta,\theta') = \begin{bmatrix} P_{11}^{1c} & 0 & 0 & 0 \\ 0 & 0 & 0 & 0 \\ 0 & 0 & P_{33}^{1c} & P_{34}^{1c} \\ 0 & 0 & P_{43}^{1c} & P_{44}^{1c} \end{bmatrix} \tag{A.19}$$

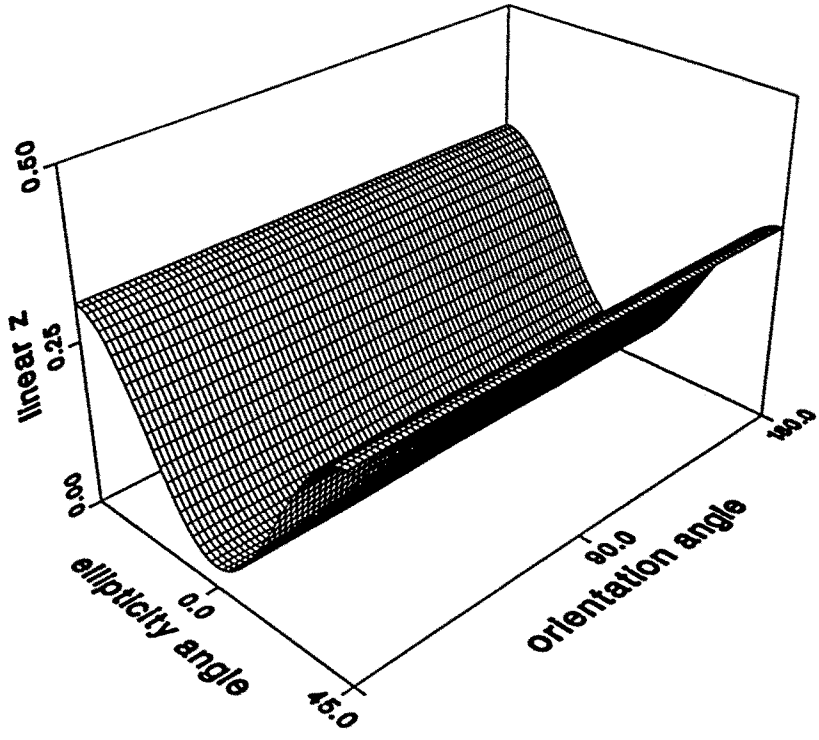

Figure 2.15b Depolarization coefficient ($\sigma_d = 0.306$ at $\psi = 180°$, $\chi = -45°$).

$$\overline{\overline{P}}^{2c}(\theta,\theta') = \begin{bmatrix} P_{11}^{2c} & P_{12}^{2c} & 0 & 0 \\ P_{21}^{2c} & P_{22}^{2c} & 0 & 0 \\ 0 & 0 & P_{33}^{2c} & 0 \\ 0 & 0 & 0 & 0 \end{bmatrix} \tag{A.20}$$

$$\overline{\overline{P}}^{1s}(\theta,\theta') = \begin{bmatrix} 0 & 0 & P_{13}^{1s} & P_{14}^{1s} \\ 0 & 0 & 0 & 0 \\ P_{31}^{1s} & 0 & 0 & 0 \\ P_{41}^{1s} & 0 & 0 & 0 \end{bmatrix} \tag{A.21}$$

$$\overline{\overline{P}}^{2s}(\theta,\theta') = \begin{bmatrix} 0 & 0 & P_{13}^{2s} & 0 \\ 0 & 0 & P_{23}^{2s} & 0 \\ P_{31}^{2s} & P_{32}^{2s} & 0 & 0 \\ 0 & 0 & 0 & 0 \end{bmatrix} \tag{A.22}$$

where the non-zero elements are given as

$$P_{11}^{o} = L_1 \left[\sin^2\theta \sin^2\theta' + \frac{\cos^2\theta \cos^2\theta'}{2} \right]$$

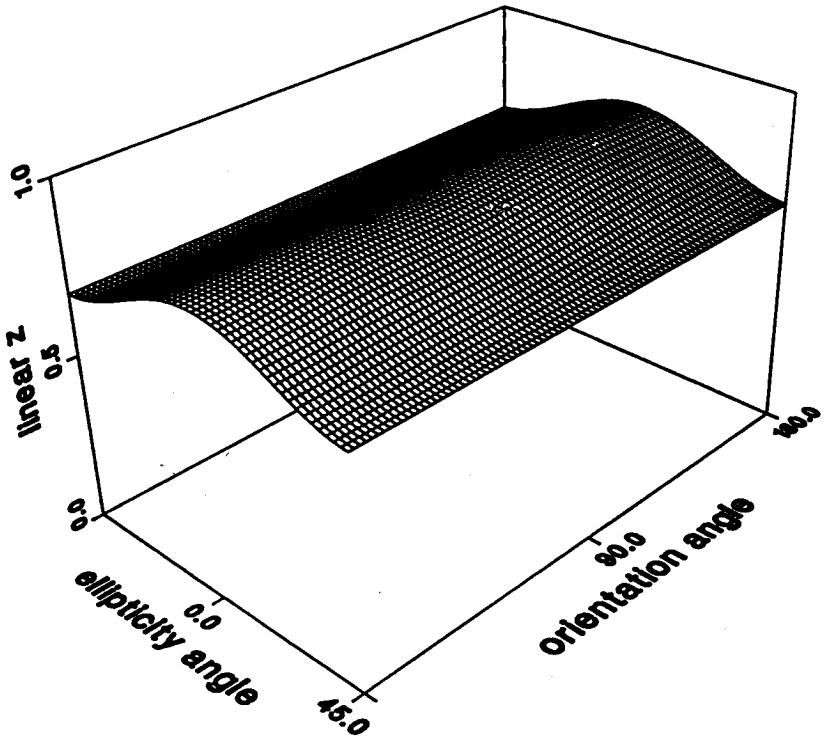

Figure 2.15c Degree of polarization.

$$+ L_2 \left[\frac{\langle \sin^4 \beta \rangle}{4} \cos^2 \theta \cos^2 \theta' + \langle \cos^4 \beta \rangle \sin^2 \theta \sin^2 \theta' + \frac{\langle \sin^2 \beta \cos^2 \beta \rangle}{2} (\cos^2 \theta \sin^2 \theta' + \sin^2 \theta \cos^2 \theta') \right] + 2L_3 \left[\langle \cos^2 \beta \rangle \sin^2 \theta \sin^2 \theta' + \langle \sin^2 \beta \rangle \frac{\cos^2 \theta \cos^2 \theta'}{4} \right] \tag{A.23}$$

$$P_{11}^{1c} = \sin \theta \sin \theta' \cos \theta \cos \theta' \left[2L_1 + \frac{3}{2} L_2 \langle \sin^2 \beta \cos^2 \beta \rangle + 2L_4 \right] \tag{A.24}$$

$$P_{11}^{2c} = \frac{1}{2} \cos^2 \theta \cos^2 \theta' \left[L_1 + L_2 \frac{\langle \sin^4 \beta \rangle}{4} + L_3 \langle \sin^2 \beta \rangle \right] \tag{A.25}$$

$$P_{12}^{o} = L_1 \frac{\cos^2 \theta}{2} + L_2 \left[\frac{\langle \sin^4 \beta \rangle \cos^2 \theta}{4} + \frac{\langle \sin^2 \beta \cos^2 \beta \rangle}{2} \sin^2 \theta \right]$$

$$+ L_3 \frac{\cos^2\theta}{2}\langle \sin^2\beta\rangle \tag{A.26}$$

$$P_{12}^{2c} = -\frac{\cos^2\theta}{2}\left[L_1 + \frac{L_2}{4}\langle \sin^4\beta\rangle + L_3\langle \sin^2\beta\rangle\right] \tag{A.27}$$

$$P_{13}^{1s} = \sin\theta \sin\theta' \cos\theta \left[L_1 + L_2\langle \sin^2\beta \cos^2\beta\rangle + L_4\right] \tag{A.28}$$

$$P_{13}^{2s} = \cos^2\theta \cos\theta' \left[\frac{L_1}{2} + L_2\frac{\langle \sin^4\beta\rangle}{8} + L_3\frac{\langle \sin^2\beta\rangle}{2}\right] \tag{A.29}$$

$$P_{14}^{1s} = \sin\theta \sin\theta' \cos\theta L_5 \tag{A.30}$$

$$P_{21}^{o} = L_1\frac{\cos^2\theta'}{2} + L_2\left[\frac{\langle \sin^4\beta\rangle \cos^2\theta'}{4} + \frac{\langle \sin^2\beta\cos^2\beta\rangle}{2}\sin^2\theta'\right] + L_3\frac{\langle \sin^2\beta\rangle}{2}\cos^2\theta' \tag{A.31}$$

$$P_{21}^{2c} = -\frac{\cos^2\theta'}{2}\left[L_1 + L_2\frac{\langle \sin^4\beta\rangle}{4} + L_3\langle \sin^2\beta\rangle\right] \tag{A.32}$$

$$P_{22}^{o} = \frac{L_1}{2} + L_2\frac{\langle \sin^4\beta\rangle}{4} + L_3\frac{\langle \sin^2\beta\rangle}{2} \tag{A.33}$$

$$P_{22}^{2c} = \frac{L_1}{2} + \frac{L_2}{8}\langle \sin^4\beta\rangle + L_3\frac{\langle \sin^2\beta\rangle}{2} \tag{A.34}$$

$$P_{23}^{2s} = -\frac{\cos^2\theta'}{2}\left[L_1 + \frac{L_2}{4}\langle \sin^4\beta\rangle + L_3\langle \sin^2\beta\rangle\right] \tag{A.35}$$

$$P_{31}^{1s} = -2\sin\theta \sin\theta' \cos\theta' \left[L_1 + L_2\langle \sin^2\beta\cos^2\beta\rangle + L_4\right] \tag{A.36}$$

$$P_{31}^{2s} = -2\cos\theta \cos^2\theta' \left[\frac{L_1}{2} + L_2\frac{\langle \sin^4\beta\rangle}{8} + L_3\frac{\langle \sin^2\beta\rangle}{2}\right] \tag{A.37}$$

$$P_{32}^{2s} = \cos\theta\left[L_1 + L_2\frac{\langle \sin^4\beta\rangle}{4} + L_3\langle \sin^2\beta\rangle\right] \tag{A.38}$$

$$P_{33}^{1c} = \sin\theta \sin\theta' \left[L_1 + L_2\langle \sin^2\beta\cos^2\beta\rangle + L_4\right] \tag{A.39}$$

$$P_{33}^{2c} = \cos\theta \cos\theta' \left[L_1 + L_2\frac{\langle \sin^4\beta\rangle}{4} + L_3\langle \sin^2\beta\rangle\right] \tag{A.40}$$

$$P_{34}^{1c} = \sin\theta \sin\theta' L_5 \tag{A.41}$$

$$P_{41}^{1s} = 2\sin\theta \sin\theta' \cos\theta' L_5 \tag{A.42}$$

$$P_{43}^{1c} = -2\sin\theta \sin\theta' L_5 \tag{A.43}$$

$$P_{44}^{o} = \cos\theta \cos\theta' \left[L_1 + L_3\langle\sin^2\beta\rangle\right] \tag{A.44}$$

$$P_{44}^{1c} = \sin\theta \sin\theta' \left[L_1 + L_4\right] \tag{A.45}$$

with L_1, L_2, L_3, L_4 and L_5 defined by

$$L_1 = \frac{9n_o}{4k^2}|T_1|^2 \tag{A.46}$$

$$L_2 = \frac{9n_o}{4k^2}|T_0 - T_1|^2 \tag{A.47}$$

$$L_3 = \frac{9n_o}{4k^2} Re\left(T_1(T_0^* - T_1^*)\right) \tag{A.48}$$

$$L_4 = \frac{9n_o}{4k^2} Re\left(T_1(T_0^* - T_1^*)\right)\left[\langle\cos^2\beta\rangle + \frac{1}{2}\langle\sin^2\beta\rangle\right] \tag{A.49}$$

$$L_5 = \frac{9n_o}{4k^2} Im\left(T_1(T_0^* - T_1^*)\right)\left[\langle\cos^2\beta\rangle - \frac{1}{2}\langle\sin^2\beta\rangle\right] \tag{A.50}$$

References

[1] Huynen, J. R., "Phenomenological theory of radar targets," 653–712, Edited by Piergirogio L. E. Uslenghi, *Electromagnetic Scattering*, Academic Press, New York, 1978.

[2] Evans, D. L., T. G. Farr, J. P. Ford, T. W. Thompson, and C. L. Werner, "Multipolarization radar images for geologic mapping and vegetation discrimination," *IEEE Trans. Geosci. Remote Sensing*, **GE–24**, 246–257, 1986.

[3] Zebker, H. A., J. J. van Zyl, and D. N. Held, "Imaging radar polarimetry from wave synthesis," *J. Geophys. Res.*, **92**, B1, 683–701, 1987.

[4] van Zyl, J. J., H. A. Zebker, and C. Elachi, "Imaging radar polarization signatures: theory and observation," *Radio Science*, **22**, 529–543, 1987.

[5] Borgeaud, M., R. T. Shin, and J. A. Kong, "Theoretical models for polarimetric radar clutter," *J. Electro. Waves Applic.*, **1**, 73–89, 1987.

[6] Wu, S.-T., and S. A. Sader, "Multipolarization SAR data for surface feature delineation and forest vegetation characterization," *IEEE Trans. Geosci. Remote Sensing*, **GE–25**, 67–76, 1987.

[7] Boerner, W.-M., B.-Y. Foo, and H. J. Eom, "Interpretation of polarimetric copolarization phase term in radar images obtained with the JPL airbone L-band SAR system," *IEEE Trans. Geosci. Remote Sensing*, **GE–25**, 77–82, 1987.

[8] Ulaby, F. T., D. N. Held, M. C. Dobson, K. C. McDonald, and T. B. A. Senior, "Relating polarization phase difference of SAR signals to scene properties," *IEEE Trans. Geosci. Remote Sensing*, **GE–25**, 83–92, 1987.

[9] Evans, D. L., T. G. Farr, J. J. van Zyl, and H. A. Zebker, "Radar polarimetry: analysis tools and applications," *IEEE Trans. Geosci. Remote Sensing*, **GE–26**, 774–789, 1988.

[10] Wen, B., L. Tsang, D. P. Winebrenner, and A. Ishimaru, "Dense medium radiative transfer theory: comparison with experiment and application to microwave remote sensing and polarimetry," *IEEE Trans. Geosci. Remote Sensing*, **GE–28**, 46–59, 1990.

[11] Tsang, L., J. A. Kong, and R. T. Shin, *Theory of Microwave Remote Sensing*, New York: Wiley–Interscience, 1985.

[12] Ishimaru, A., and R. L.-T. Cheung, "Multiple scattering effects on wave propagation due to rain," *Ann. Telecommunication*, **35**, 373–379, 1980.

[13] Tsang, L., M. C. Kubacsi, and J. A. Kong, "Radiative transfer theory for active remote sensing of a layer of small ellipsoidal scatterers," *Radio Science*, **16**, 321–329, 1981.

[14] Ishimaru, A., D. Lesselier, and C. Yeh, "Multiple scattering calculations for nonspherical particles based on the vector radiative transfer theory," *Radio Science*, **19**, 1356–1366, 1984.

[15] Ishimaru, A., and C. W. Yeh, "Matrix representations of the vector radiative transfer equations for randomly distributed nonspherical particles," *J. Opt. Soc. Am. A.*, **1**, 359–364, 1984.

[16] Tsang, L., J. A. Kong, and R. T. Shin, "Radiative transfer theory for active remote sensing of a layer of nonspherical particles," *Radio Science,* **19**, 629–642, 1984.

[17] Tsang, L., "Thermal emission of nonspherical particles," *Radio Science,* **19**, 966–974, 1984.

[18] Tsang, L., and A. Ishimaru, "Radiative wave equations for vector electromagnetic propagation in dense nontenuous media," *J. Electro. Waves Applic.,* **1**, 52–72, 1987.

[19] Tsang, L., and A. Ishimaru, "Radiative wave and cyclical transfer equation for dense nontenuous media," *J. Opt. Soc. Am.,* **2**, 2187–2194, 1987.

[20] Ding, K. H., and L. Tsang, "Effective propagation constants of dense nontenuous media with multi–species of particles," *J. of Electro. Waves Applic.,* **2**, 757–777, 1988.

[21] Ding, K. H., and L. Tsang, "Effective Propagation Constants in media with densely distributed dielectric particles of multiple sizes and permittivities," *Progress in Electromagnetics Research,* Chapter 3, **1**, 241–295, edited by J. A. Kong, Elsevier Science, 1989.

[22] Tsang, L., "Dense media radiative transfer theory for dense discrete random media with particles of multiple sizes and permittivities," submitted to *Progress in Electromagnetics Research,* 1988.

[23] Chandrasekhar, S., *Radiative Transfer*, New York, Dover, 1960.

[24] Ishimaru, A., and Y. Kuga, "Attenuation constant of coherent field in a dense distribution of particles," *J. Opt. Soc. Am.,* **72**, 1317–1320, 1982.

[25] Kuga, Y., *Laser Light Propagation and Scattering in a Dense Distribution of Spherical Particles,* Ph.D. Dissertation, University of Washington, Seattle, 1983.

[26] Kuga, Y., and A. Ishimaru, "Retroreflectance from a dense distribution of spherical particles," *J. Opt. Soc. Am. A.,* **1**, 831–835, 1984.

[27] Lebowitz, J. L., "Exact solution of generalized Percus-Yevick equation for a mixture of hard spheres," *Phys. Rev.,* **133**, A895–899, 1964.

[28] Baxter, R. J., "Ornstein-Zernike relation for a disordered fluid,"

Aust. J. Phys., **21**, 563–569, 1968.

[29] Baxter, R. J., "Ornstein-Zernike relation and Percus-Yevick approximation for a fluid mixtures," *J. Chem. Phys.*, **52**, 4559–4562, 1970.

[30] Barker, J. A., and D. Henderson, "Molecular Monte Carlo values for the radial distribution function of a system of fluid hard spheres," *Molecular Physics*, **21**, 187–191, 1971.

[31] Mandt, C. E., *Microwave propagation and scattering in a dense distribution of spherical particles*, M.S. thesis, University of Washington, 1987.

[32] Lang, R., "Electromagnetic backscattering from a sparse distribution of lossy dielectric scatterers," *Radio Science*, **16**, 15–33, 1981.

[33] Shin, R. T., and J. A. Kong, "Radiative transfer theory for active remote sensing of a homogeneous layer containing spherical scatterers," *J. Appl. Phys.*, **52**, 4221–4230, 1981.

[34] Ishimaru, A., *Wave Propagation and Scattering in Random Media*, Vol. I & II, Academic Press, New York, 1978.

[35] Deirmendjian, D., *Electromagnetic Scattering on Spherical Polydispersions*, Elsevier, New York, 1969.